

ISTANBUL TECHNICAL UNIVERSITY ★ GRADUATE SCHOOL OF SCIENCE
ENGINEERING AND TECHNOLOGY

**STABILITY ANALYSIS OF NONLINEAR
SYSTEMS AND UPSET RECOVERY STRATEGIES
FOR AGILE MANEUVERING AIRCRAFT**

M.Sc. THESIS

Batuhan HOŞTAŞ

Department of Aeronautics and Astronautics

Aeronautics and Astronautics Programme

JUNE 2018

**STABILITY ANALYSIS OF NONLINEAR
SYSTEMS AND UPSET RECOVERY STRATEGIES
FOR AGILE MANEUVERING AIRCRAFT**

M.Sc. THESIS

**Batuhan HOŞTAŞ
(511161110)**

Department of Aeronautics and Astronautics

Aeronautics and Astronautics Programme

Thesis Advisor: Asst. Prof. Nazım Kemal ÜRE

JUNE 2018

**NONLİNEER SİSTEMLERİN KARARLILIK ANALİZİ
VE ÇEVİK MANEVRA YAPAN UÇAKLAR İÇİN
GÜVENLİ UÇUŞA DÖNME STRATEJİLERİ**

YÜKSEK LİSANS TEZİ

**Batuhan HOŞTAŞ
(511161110)**

Uçak ve Uzay Mühendisliği Anabilim Dalı

Uçak ve Uzay Mühendisliği Programı

Tez Danışmanı: Asst. Prof. Nazım Kemal ÜRE

HAZİRAN 2018

Batuhan HOŞTAŞ, a M.Sc. student of ITU Graduate School of Science Engineering and Technology 511161110 successfully defended the thesis entitled “STABILITY ANALYSIS OF NONLINEAR SYSTEMS AND UPSET RECOVERY STRATEGIES FOR AGILE MANEUVERING AIRCRAFT”, which he/she prepared after fulfilling the requirements specified in the associated legislations, before the jury whose signatures are below.

Thesis Advisor : **Asst. Prof. Nazım Kemal ÜRE**
Istanbul Technical University

Jury Members : **Asst. Prof. Emre KOYUNCU**
Istanbul Technical University

Asst. Prof. A. Ersan OĞUZ
National Defense University

.....

Date of Submission : **4 May 2018**

Date of Defense : **4 June 2018**





To Hilal and my family,



FOREWORD

This thesis is one of the outcomes of my studies under the grant agreement 315M341 by Scientific and Technological Research Council of Turkey (Turkish: TÜBİTAK) . During this project, I gained both theoretical and practical experience in flight control systems and flight safety concepts. Although, I still cannot claim to be an expert on these topics, I acquired a great deal of knowledge and open up my horizon in a short period of time. This project helped me to gain academic thinking as well as to enlarge my perspective as an engineer in order to think analytically and solve any kind of problems within its own context.

I am grateful to all teachers and students from Control and Avionics Lab and Aerospace Research Center who took part in this project and helped to take it one step further. In particular, I would like to thank Asst. Prof. Nazım Kemal ÜRE for giving me the opportunity to take part in a TÜBİTAK project. I thank Mehmet Uğur Akçal and Anıl Yıldız for their help whenever I needed as well as for being the perfect team friends in publishing great papers. Last but not least, I would like to thank Hilal Gülşen and my family for their moral support.

June 2018

Batuhan HOŞTAŞ

TABLE OF CONTENTS

	<u>Page</u>
FOREWORD	ix
TABLE OF CONTENTS	xi
ABBREVIATIONS	xiii
SYMBOLS	xv
LIST OF TABLES	xvii
LIST OF FIGURES	xix
SUMMARY	xxiii
ÖZET	xxv
1. INTRODUCTION	1
1.1 Purpose of Thesis	1
1.2 Literature Review	2
1.3 Contribution and Overview of the Thesis.....	3
2. UPSET RECOVERY STRATEGIES FOR AGILE MANEUVERING AIRCRAFT	5
2.1 Simulation Model	5
2.2 Controller Derivations	6
2.2.1 Linear Angular Rate Regulator.....	6
2.2.2 NDI Controller for Angular Rates.....	7
2.2.3 NDI Controller for Angle of Attack, Sideslip and Bank Angle	11
2.2.4 Switching Controller	13
2.3 Simulation Results.....	13
2.3.1 Linear Controller	14
2.3.2 Single Loop NDI Controller (C_1)	17
2.3.3 Double Loop NDI Controller (C_2).....	20
2.3.4 Switching NDI Controller (C_3).....	24
2.4 Middle State Approach.....	30
3. NEURAL NETWORK APPROACH FOR RECOVERABILITY ENVELOPE ESTIMATION	33
3.1 Preliminaries.....	33
3.2 Neural Network Model.....	33
3.3 Results	34
4. CONCLUSIONS AND RECOMMENDATIONS	41
REFERENCES	43
CURRICULUM VITAE	45



ABBREVIATIONS

App	: Appendix
GTM	: Generic Transport Model
HI-FI	: High Fidelity
LOC	: Loss of Control
LQR	: Linear Quadratic Regulator
NDI	: Nonlinear Dynamic Inversion
NED	: North-East-Down
PI	: Proportional-Integral





SYMBOLS

α	: Angle of attack
A_x, A_y, A_z	: Forces in x,y,z axis
b	: Wing span
β	: Sideslip angle
C_l, C_m, C_n	: Roll, pitch, yaw moment coefficients
$\delta_e, \delta_a, \delta_r,$ δ_{lef}	: elevator, aileron, rudder, leading edge flap deflection
δ_T	: Throttle position
h	: Altitude
h_x	: Engine angular momentum
I	: Moment of inertia
L, M, N	: Roll, pitch, yaw moment
ω	: Body angular velocity vector
\mathbf{p}	: Position vector
$\mathbf{P, Q, R}$: Roll, pitch, yaw rates
ϕ, θ, ψ	: Roll, pitch, yaw angles
\mathbf{q}	: Quaternion vector
\bar{q}	: Dynamic pressure
S	: Reference area
\mathbf{u}	: Input vector
\mathbf{V}_T	: Total velocity
\mathbf{x}	: State vector



LIST OF TABLES

	<u>Page</u>
Table 2.1 : Simulation stop conditions and the corresponding final simulation status.	14





LIST OF FIGURES

	<u>Page</u>
Figure 2.1 : Block diagram of NDI based angular rate controller.....	7
Figure 2.2 : Description of the table inversion for elevator deflection determination.	11
Figure 2.3 : Block diagram of the double loop NDI controller.	11
Figure 2.4 : Block diagram of the switching mechanism.....	13
Figure 2.5 : Angular rate and reference-command input time history results obtained from the simulations where LQR is employed for the angular rate regulation. Initial roll rate, pitch rate, yaw rate, and angle of attack are -1.5 rad/s, -1 rad/s, 2 rad/s and 12°, respectively..	15
Figure 2.6 : Relative airspeed, angle of attack, sideslip angle, and load factor time histories obtained from the simulations where LQR is employed for the angular rate regulation.	15
Figure 2.7 : The angular rate envelopes obtained for the linear quadratic regulator while considering 4° and 24° initial angle of attack scenarios: Green nodes represents (0-8)s regulation time, black nodes represents (8-15)s regulation time, and blue nodes represents (15-100)s regulation time.	16
Figure 2.8 : The number of regulation nodes vs. regulation time interval histograms obtained for the linear quadratic regulator while considering 4° and 24° initial angle of attack scenarios	16
Figure 2.9 : Angular rate and reference-command input time history results obtained from the simulations where C_1 is employed for the angular rate regulation. Initial roll rate, pitch rate, yaw rate, and angle of attack are -1.5 rad/s, -1 rad/s, 2 rad/s and 12°, respectively..	17
Figure 2.10 : Relative airspeed, angle of attack, sideslip angle, and load factor time histories obtained from the simulations where C_1 is employed for the angular rate regulation.....	18
Figure 2.11 : Flight trajectory obtained from the simulations where C_1 is employed for the angular rate regulation.	18
Figure 2.12 : The angular rate envelopes obtained for C_1 while considering 4° and 24° initial angle of attack scenarios: Green nodes represents (0-8)s regulation time, black nodes represents (8-15)s regulation time, blue nodes represents (15-100)s regulation time and red nodes represents regulation fails.....	19
Figure 2.13 : The angular rate envelopes obtained for C_1 while considering 36° and 72° initial angle of attack scenarios: Green nodes represents (0-8)s regulation time, black nodes represents (8-15)s regulation time, blue nodes represents (15-100)s regulation time and red nodes represents regulation fails.	19

Figure 2.14: The number of regulation nodes vs. regulation time interval histograms obtained for C_1 while considering 4° and 24° initial angle of attack scenarios.	20
Figure 2.15: The number of regulation nodes vs. regulation time interval histograms obtained for C_1 while considering 36° and 72° initial angle of attack scenarios.	20
Figure 2.16: Relative airspeed, angle of attack, sideslip angle, angular rate, and load factor time histories obtained from the simulations where C_2 is employed. Initial roll rate, pitch rate, yaw rate, and angle of attack are 1.75 rad/s, -0.75 rad/s, 0.75 rad/s and 12° , respectively.	21
Figure 2.17: Reference-command input time history results obtained from the simulations where C_2 is employed. Initial roll rate, pitch rate, yaw rate, and angle of attack are 1.75 rad/s, -0.75 rad/s, 0.75 rad/s and 12° , respectively.	22
Figure 2.18: Flight trajectory obtained from the simulations where C_2 is employed for the angular rate regulation.	22
Figure 2.19: The angular rate envelopes obtained for C_2 while considering 4° and 24° initial angle of attack scenarios: Green nodes represents (0-8)s regulation time, black nodes represents (8-15)s recovery time, and blue nodes represents (15-100)s.	23
Figure 2.20: The angular rate envelopes obtained for C_2 while considering 36° and 72° initial angle of attack scenarios: Green nodes represents (0-8)s regulation time, black nodes represents (8-15)s recovery time, and blue nodes represents (15-100)s.	23
Figure 2.21: Trajectory plot for C_3 . Initial angle of attack is 36° and $\omega = [1, 0.5, -3]^T$	24
Figure 2.22: Relative airspeed, angle of attack, sideslip angle, angular rate, and load factor time histories obtained from the simulations where C_3 is employed. Initial roll rate, pitch rate, yaw rate, and angle of attack are 1.75 rad/s, -0.75 rad/s, 0.75 rad/s and 12° , respectively.	25
Figure 2.23: Reference-command input time history results obtained from the simulations where C_3 is employed. Initial roll rate, pitch rate, yaw rate, and angle of attack are 1.75 rad/s, -0.75 rad/s, 0.75 rad/s and 12° , respectively.	25
Figure 2.24: Flight trajectory obtained from the simulations where C_3 is employed for the angular rate regulation.	26
Figure 2.25: The angular rate envelopes obtained for C_3 while considering 4° and 24° initial angle of attack scenarios: Green nodes represents (0-8)s recovery time, black nodes represents (8-15)s recovery time, blue nodes represents (15-100)s recovery time and red nodes represents recovery fails.	26
Figure 2.26: The angular rate envelopes obtained for C_3 while considering 36° and 72° initial angle of attack scenarios: Green nodes represents (0-8)s recovery time, black nodes represents (8-15)s recovery time, blue nodes represents (15-100)s recovery time and red nodes represents recovery fails.	26

Figure 2.27: The number of recovery nodes vs. recovery time interval histograms obtained for C_3 while considering 4° and 24° initial angle of attack scenarios.	27
Figure 2.28: The number of recovery nodes vs. recovery time interval histograms obtained for C_3 while considering 36° and 72° initial angle of attack scenarios.	27
Figure 2.29: Percentage of recovery nodes vs. angle of attack graph of linear and C_1 (NDI PQR) controllers.	28
Figure 2.30: Percentage of recovery nodes vs. angle of attack graph of C_2 (NDI ABP), C_3 (switching), and C_4 (relaxed switching) controllers..	29
Figure 2.31: Lift coefficient distribution with respect to angle of attack, where $\delta_e = 0$. This curve is obtained from the aerodynamic database of the Hi-Fi F-16 model in this study.....	29
Figure 2.32: Average recovery time vs. angle of attack graph of C_2 (NDI ABP), C_3 (switching), and C_4 (relaxed switching) controllers	30
Figure 2.33: Illustration of reference generation.....	30
Figure 2.34: Optimal time paths for regulation of angular rates	31
Figure 3.1 : Neural network scheme for 4-class case.....	34
Figure 3.2 : Neural network scheme for 2-class case.....	34
Figure 3.3 : Confusion matrix for 4-class case.....	35
Figure 3.4 : Error distribution for 4-class case	36
Figure 3.5 : Receiver operating characteristic for 4-class case	37
Figure 3.6 : Confusion matrix for 2-class case.....	38
Figure 3.7 : Error distribution for 2-class case	39
Figure 3.8 : Receiver operating characteristic for 2-class case	40



STABILITY ANALYSIS OF NONLINEAR SYSTEMS AND UPSET RECOVERY STRATEGIES FOR AGILE MANEUVERING AIRCRAFT

SUMMARY

This thesis investigates the upset recovery problem of aircrafts as well as stability analysis of general nonlinear systems. In order to deal with upset recovery problem, the strategies which contains nonlinear control techniques are adopted. In order to validate through comparison, linear control technique which make use of linear quadratic regulator is also implemented. As a nonlinear control techniques nonlinear dynamic inversion (NDI) based angular rate regulator and double loop NDI controller for angle of attack, sideslip and bank angle are derived for High fidelity F-16 aircraft model. The choice of aircraft model enabled us to observe conditions with high angular rates which can be encountered in agile maneuver executions.

Implemented controllers are evaluated through a novel framework where the recovery envelopes and recovery times are used as the performance criteria. Three dimensional recovery envelopes are constructed using three body angular rates which are used as initial points for simulations and included or excluded to recovery envelopes based on the success in recovery attempt. Successful recovery conditions are restricted so that the aircraft would not count as recovered if it exceed structural or altitude limits along with the constraints employed in actuator models. Based on the evaluations which are made by the proposed framework, another strategy is proposed which adopts the strong sides of single loop and double loop NDI controllers such that it utilizes the single loop NDI controller until the high angular rates are regulated below some predetermined threshold, then uses the double loop NDI controller to recover aerodynamic angles. This new strategy is called as switching NDI controller and its performance superiority is validated using the proposed framework.

Thereafter conducting analysis based on simulation study, another approach is implemented to mitigate the computational burden which comes along with the simulations. Neural network model is constructed to reproduce the recoverability envelopes obtained via simulations. By this way, recoverability envelopes are created with high fidelity using only small portion of the whole simulations executed before.



NONLİNEER SİSTEMLERİN KARARLILIK ANALİZİ VE ÇEVİK MANEVRA YAPAN UÇAKLAR İÇİN GÜVENLİ UÇUŞA DÖNME STRATEJİLERİ

ÖZET

Bu tez kapsamında, güvensiz uçuş rejimine girmiş hava taşıtları için güvenli uçuşa dönüş problemi ve genel nonlinear sistemlerin kararlılık analizi irdelenmektedir. Güvensiz uçuş rejimi olarak tabir edilen durumlarda son derece bağlaşıklık ve lineer olmayan dinamikler sisteme hakimdir. Bağlaşıklık ve lineer olmayan dinamikler ise klasik ya da modern lineer kontrol teknikleri ile ele alınması oldukça güçtür. Bu tip kontrolcüler nonlinear dinamiklere yakalamada düşük performansa sahiptirler. Bu sebeple, güvensiz uçuş rejimine girmiş hava taşıtlarının, güvenli uçuşa dönmesi için nonlinear kontrol tekniklerini içeren stratejiler benimsenmiştir.

Bu tezin odağında çevik manevra yapan uçakların karşılaşılabileceği güvensiz uçuş koşulları vardır. Bu sebeple, bu tezin kapsamında, güvensiz uçuş rejimleri, yüksek açısız hız değerlerini içeren uçuş koşulları olarak tanımlanmıştır. Bu uçuş rejimlerini kapsayacak simülasyon çalışmaları yürütebilmek adına çevik manevra kabiliyetine sahip bir uçak modeli üzerinde çalışmak gereklidir. Bu bağlamda, simülasyon modeli olarak yüksek duyarlılıklı F-16 modeli kullanılmıştır. Bu model güvensiz uçuş rejimlerindeki dinamikleri de içeren bir aerodinamik veritabanına sahiptir.

Daha önce de bahsedildiği gibi güvenli uçuşa dönüş problemi nonlinear kontrol teknikleri ile ele alınmıştır. Buna karşın, bu problemi çözme konusunda kontrol stratejilerinin performanslarının değerlendirilmesi açısından hem lineer hem de lineer olmayan kontrol teknikleri sunulmuş ve uygulanmıştır. Bu bağlamda, doğrusal karesel regülatör, tek çevrim nonlinear ters dinamik bazlı açısız hız regülatörü ve çift çevrim nonlinear ters dinamik bazlı aerodinamik açı regülatörü oluşturulmuştur. Bunlara ek olarak, en son bahsi geçen tek çevrim nonlinear ters dinamik bazlı açısız hız regülatörü ve çift çevrim nonlinear ters dinamik bazlı aerodinamik açı regülatörünün anahtarlamalı olarak çalıştığı, anahtarlamalı nonlinear ters dinamik kontrolcüsü önerilmiştir. Tüm kontrolcü çıkarımları, gerekli uçuş denklemleri de detaylı olarak ele alınarak açık bir şekilde sunulmuştur.

Oluşturulan tüm kontrol stratejileri, bu çalışma kapsamında önerilen bir sistem ile değerlendirilmiştir. Bu sistem, kullanılan kontrol stratejilerinin güvensiz uçuş rejiminden güvenli uçuş koşullarına geçişte harcadıkları süreyi ve de başarılı bir şekilde güvenli uçuş koşullarına taşınabilen başlangıç koşullarının oluşturduğu zarfı performans kriteri olarak ele almaktadır. Burada uçağın gövde eksenindeki üç açısız hız değeri (yuvarlanma hızı, yunuslama hızı, yalpalama hızı) zarfı oluşturmak için kullanılmaktadır. Bu sebeple, geniş bir yelpazede yüksek sayıda açısız hız kombinasyonları sisteme başlangıç değeri olarak verilmiş ve bahsi geçen kontrolcülerin bu koşullardan ne kadarını güvenli uçuş rejimine döndürebildiği takip edilmiştir. Ayrıca bütün zarflar farklı hücum açıları değerleri için tekrarlanmış

ve böylelikle hücum açısının da güvenli uçuşa dönüşteki etkisi incelenmiştir. Bu çalışma kapsamında hangi kontrolcülerin geniş toparlanma zarfına, hangilerinin ise daha dar toparlanma zarfına sahip olduğuna bakılarak kontrolcülerin performansları karşılaştırılmıştır.

Tüm kontrolcüler geniş açısız hız zarflarında ve çeşitli hücum açılarındaki Monte Carlo simülasyonlarına tabi tutulmuş ve bahsi geçen performans kriterlerine göre değerlendirilmiştir. Buna göre, lineer kontrolcü beklendiği gibi çok sınırlı bir toparlanma zarfına sahiptir. Toparlanma hızı açısından başarılı bir performans göstermesi ise optimal kontrol tabanlı bir kontrolcü olması ile uyumaktadır. Diğer yandan en geniş toparlanma zarfına sahip kontrolcü ise tek çevrim nonlineer ters dinamik bazlı açısız hız regülatörüdür. Toparlanma hızı ise hücum açısıyla ters orantılı bir karakter sergilemektedir. Geniş toparlanma zarfına sahip olmasına karşın bu kontrolcünün aerodinamik açıları kontrol edebilme yetisi bulunmamaktadır. Her ne kadar açısız hızları regüle etmede çok üstün bir performans gösterse de, tam anlamıyla güvensiz uçuş rejiminden kurtulma problemine yanıt vereceği söylenemez. Buna karşın bu işlevi yerine getirebilecek çift çevrim nonlineer ters dinamik bazlı aerodinamik açı regülatörü ise nonlineer açısız hız regülatörüne karşın çok daha küçük bir zarfta etkin olabilmektedir. Bu sonuçlar vesilesi ile önerilen anahtarlamalı nonlineer ters dinamik kontrolcüsü ise geniş bir zarfta açısız hızları regüle etmeyi başarmış, açısız hızları regüle olmuş sistemde de başarılı bir şekilde aerodinamik açı regülasyonunu sağlayabilmiştir. Ek olarak, anahtarlamalı kontrolcünün anahtar değişim eşiğinin güvenli uçuş rejimine dönüş sürelerine etkisi gözlemlenmiştir. Öyle ki, farklı bir eşik değeri ile aynı şartlar altında Monte Carlo simülasyonları koşulduğunda toparlanma sürelerinde ortalama on saniyeye varan kısalma görülmüştür. Kontrol kaybı durumlarında, süre çok kırıktır bir parametredir. Uçağın güvensiz uçuş rejiminde kaldığı her saniye daha da geri dönülemez uçuş rejimlerine girmesine sebep verebilmektedir. Bu sebeple de kontrolcüler için önerilen performans kriterlerinden biri toparlanma süresi olarak belirlenmiştir. Bahsi geçen son çalışmanın geliştirilebilir ve bir optimizasyon çalışmasına döndürülebilir olması, geleceğe yönelik akademik araştırma olanağı doğurması demektir ve bu bağlamda önemlidir.

Güvenli uçuşa dönüş için değerlendirilen bir diğer strateji ise iki basamaklı toparlanma stratejisidir. Buna göre açısız hızlar ve aerodinamik açıları doğrudan regüle edilmeye çalışılmayıp, arada bir uçuş koşulu üzerinden geçilerek tam regülasyona yönlendirilmektedir. Dar bir zarfta test edilen bu yaklaşımda bazı noktalar için toparlanma süresini kısaltan ara durum koşullarının bulunduğu gösterilmiştir. Bu koşulların neredeyse tamamında yalpalama ve yunuslama hızları hedeflenen son değer ile aynı olup sıfırken yuvarlanma hızında farklı değerler gözlemlenebilmiştir. Bu çalışmanın güvenli uçuşa dönüşü hızlandırma konusunda yol göstericiliğinin yanı sıra, güvenli uçuşa dönüşün dinamikleri konusunda da bilgilendirici olmuştur. Öyle ki, güvenli uçuşa dönüş açısından, yunuslama ve yalpalama hızlarının düşürülmesi, yuvarlanma hızının düşürülmesine göre daha fazla önem arz etmektedir. Dolayısıyla, kontrol yüzeylerinin öncelikli olarak sadece yunuslama ve yalpalama hızlarının düşürülmesi için kullanılması güvenli uçuş zarfına dönüşte zaman avantajı sağlayabilmektedir.

Yüksek uygunluklu 6 serbestlik dereceli bir F-16 modeli ve nonlineer kontrolcüler düşünüldüğünde Monte Carlo simülasyonları bazlı yapılan kararlılık analizi çalış-

maları hesaplama yükü ve zaman açısından oldukça maliyetlidir. Bu sebeple, aynı çalışmaların daha az hesaplama yükü ve zaman ile üretilebilmesi açısından yapay sinir ağı bazlı bir çalışma yürütülmüştür. Bu çalışma kapsamında 1 giriş, 1 çıkış ve 4 gizli katmandan oluşan 2 ayrı model oluşturulmuştur. Modellerden birinin amacı 4 farklı sınıflandırma yapmasıdır. Bu sınıflar, güvenli uçuşa dönüşün yanı sıra güvenli uçuşa dönüşün başarısız olması durumunda hangi sebepten başarısız olduğunu da belirten durumları ifade etmektedir. Güvenli uçuşa dönüşte başarısızlık durumları hız şartının, irtifa şartının ve yük faktörü şartının ihlal edildiği durumlardır. Bu üç farklı durumun yanı sıra başarılı olduğu durumlarla birlikte 4 ayrı sınıflandırma yapılmış ve oluşturulan ilk model bu sınıflandırmayı yapmak üzerine tasarlanmıştır. Diğer modelin amacı ise 2 farklı sınıflandırma yapmasıdır. Bunlar ise güvenli uçuşa dönüşün başarılı ve başarısız olduğu durumlar olarak tanımlanmıştır. Modellerin eğitimi için daha önce yapılan Monte Carlo simülasyonlarının verileri kullanılmıştır. Burada önemli olan nokta ise eğitim için bu verilerinin sadece %20'sinin kullanılmış olmasıdır. Hesaplama yükü ve zaman açısından maliyeti düşürme de bu şekilde gerçekleşmiştir. Verilerin sadece küçük bir kısmı kullanılarak %87 oranında benzer toparlanma zarfları elde edilmiştir. Bununla birlikte, sınıflandırmada karşılaşılan hata oranları ve hangi sınıfların daha kolay hangi sınıfların daha zor ayrıştırıldığına yönelik sonuçlar da ortaya konmuştur. Hata oranlarının düşük olması, parametrelerin optimizasyonu ve sınıflandırma koşullarının sıkılaştırılması gibi çalışmalar yapılarak modelin daha yüksek başarı oranlarına çıkabileceği konusunda umut vermekte ve ileriye yönelik çalışma imkanları sunmaktadır.



1. INTRODUCTION

In this thesis, we consider a problem of upset recovery for aircrafts and stability analysis of systems with nonlinear dynamics. Unlike nominal flight conditions, dynamics of the aircraft cannot be compensated with their linearized versions in upset conditions since these conditions unveil the highly nonlinear, coupled nature of the state equations. Therefore, linear control techniques are not sufficient for such problem.

In order to overcome the nonlinear and coupled nature of aircraft dynamics, nonlinear control techniques are considered in this study. Linear control techniques are also investigated to observe the effectiveness compared to nonlinear control techniques. We approach to the problem considering fighter aircrafts which are capable of executing agile maneuvers such that larger upset space can be investigated. In this study, upset space definition is based on the angular velocities of an aircraft which are crucial inputs for aircraft maneuvers. Therefore, recovery strategies are composed mainly within the scope of angular velocities.

Recovery strategies implemented in this study contains nonlinear dynamic inversion(NDI) control technique. In spite of the fact that NDI lacks robustness, aircraft model used in this study assumed to have no parametric uncertainty or external noise. In addition, strategies given in this study are prone to be implemented using robust control techniques such as sliding mode control.

Recoverability analysis is conducted using the previously mentioned recovery strategies. Two approaches are utilized to perform the analysis. First one is based on the extensive Monte Carlo simulations, second one is based on the neural networks.

1.1 Purpose of Thesis

Loss-of-Control (LOC) is the main cause of fatal accidents in aviation according to the past statistics on this manner [1–4]. For this reason, civil aviation community

fastidiously handled the LOC and carried out substantial work on training for upset recovery situations aided with simulation platforms [5, 6]. Despite the training pilots take for upset recovery, instinctual commands given by pilot and a response capability of a human cannot be acknowledged as sufficient to handle LOC, especially, accidents are taken into account caused by incorrect pilot commands [7]. This argument is even more realistic in case of a fighter aircraft. The reason for that is fighter aircraft operations, such as executing agile maneuvers which may cause the aircraft dragged into unsafe flight regimes such as spin and stall [8]. Since spin and stall may lead to LOC, vehicle upset is considered as one of the main source for the LOC [9]. Therefore, study of upset recovery strategies and creating autonomous upset recovery systems are crucial.

1.2 Literature Review

Remarkable amount of study is present in the literature considering the aircraft upset recovery. Engelbrecht et al. [10] offer an upset recovery system for a transport class aircraft using a state machine approach. They make use of natural damping of the aircraft for angular velocity and aerodynamic angle recovery. Lombaerts et al. [11] present a stall recovery system which utilizes energy flow to determine proper control signals. However, these methods lack recovery capability for upset conditions encountered whilst performing agile maneuvers.

Rao and Sinha [12] studied the spin recovery problem using a sliding mode controller. However, they validate the performance of their recovery strategy using only a couple of spin scenarios, making it difficult to accept as a generalized strategy. Similarly, Raghavendra et al. [13] present spin recovery strategy using a nonlinear dynamic inversion controller which get through to required state via two-step reference states. Nevertheless, proposed strategy is only validated for just one spin scenario. Dongmo [14] uses feedback linearization and high order sliding mode controller to overcome post LOC conditions. Even so, states and controls are limited such that the proposed strategy can only be confirmed on a narrow flight envelope.

Crespo et al. [15] propose an upset recovery strategy and validate it on seven different upset scenarios to derive a recoverable flight envelope. Gill et al. [16] study the performance of the flight controllers of Generic Transport Model (GTM) [17] outside

its nominal flight conditions. In this study, linear quadratic regulator(LQR) controller with gain scheduling is implemented. However, these approaches are not validated for conditions which the agile aircrafts might encounter.

1.3 Contribution and Overview of the Thesis

In this thesis, upset recovery framework is proposed in which the implemented controllers are evaluated. Using this framework, controllers are evaluated based on two main criteria. One of them is the angular velocity envelope extent of the controllers, whereas the other is the time consumption for recovery procedure. Angular velocity envelopes are obtained by running the simulations for an extensive set of roll rate, pitch rate and yaw rate values where the achievement of angular rate regulations, as well as angle of attack, sideslip and bank angle regulations are considered as successful recovery. On the other hand, performance on the time of recoveries are presented via time histograms with number of recovery nodes(angular velocity triples) vs. recovery time.

Although numerous nonlinear control techniques and linear control techniques such as LQR are proposed as part of recovery strategies in the past, different strategies are not subjected to comparative studies within a study. In this thesis, LQR controller, NDI based angular rate regulator, double loop NDI controller and NDI based switching controller are subjected to comparative study within a large envelope. Comparative studies reveal the fact that nonlinear controllers are superior to linear controllers within the context of upset recovery problem. On the other hand, different performance characteristics between NDI based angular rate regulator and a double loop NDI controller made way to come up with a new strategy employing NDI based switching controller which make use of the strong sides of the aforementioned nonlinear controllers. Switching controller initially performs the angular rate regulation and continue with attitude regulation satisfying the control of aerodynamic angles as double loop NDI and achieving the larger envelope extent as NDI based angular rate regulator.

To sum up, recovery time and recovery envelope extent based framework is proposed in order to evaluate the controllers. Several approaches are compared and their strong

and weak sides are determined. Using the results obtained by the comparative study, NDI based switching controller is proposed.

Finally, computational burden of the nonlinear stability analysis due to Monte Carlo simulations are eliminated using a neural network approach. This approach pave the way for generalizing the analysis to whole state space using only a limited number of simulation data.

The outline of this thesis is as follows:

In chapter 2, upset recovery study for an agile aircraft is given. The simulation model is briefly presented whereas linear and nonlinear controller derivations are given in detail. Results of the extensive simulations are given in terms of aforementioned framework. In the end of results section, another case has also been taken into account where the switching threshold is changed. Additional recovery strategy idea is introduced where the recovery is executed in two step in which the final state is achieved through a middle state.

In chapter 3, a neural network model is introduced to conduct stability analysis. Recoverability problem is considered as a supervised classification problem by using the previously gathered simulation data. Recoverability envelopes are obtained using the trained neural network model. Neural network's result are presented using confusion matrices, error histograms and receiver operator characteristics.

Chapter 4 concludes the thesis and give some future recommendations upon this research area.

2. UPSET RECOVERY STRATEGIES FOR AGILE MANEUVERING AIRCRAFT

In this chapter, investigation of the upset recovery strategies for agile maneuvering aircraft is carried out. Recoverability envelope based analysis is performed for linear and nonlinear control laws using a high fidelity F-16 aircraft model.

2.1 Simulation Model

Due to consideration of upset conditions which require the availability of offnominal dynamics, high-fidelity (Hi-Fi) non-linear F-16 model [18] is used in this study. The Hi-Fi F-16 model provides a large aerodynamic data [19] and actuator models for elevator, aileron, rudder and engine as well as a leading edge flap. Different look-up tables are used for different power settings such as "idle", "military", and "maximum" [20]. The system assumed to have no uncertainties in the parameters. There is no noise or disturbances modeled for the system. Standard atmosphere model has been used throughout the all simulation studies.

Aircraft's state vector is given in Eq. 2.1 as:

$$\mathbf{x}^T = [V_T, \alpha, \beta, \mathbf{q}^T, \boldsymbol{\omega}^T, \mathbf{p}^T] \in \mathbb{R}^{13} \quad (2.1)$$

where V_T is the total velocity with respect to the aircraft body, α and β are angle of attack and sideslip angle, respectively. $\mathbf{q}^T = [q_0, q_1, q_2, q_3] \in \mathbb{R}^4$ is the aircraft attitude quaternion which represents the orientation of the aircraft with respect to the North-East-Down (NED) frame, $\boldsymbol{\omega}^T = [P, Q, R] \in \mathbb{R}^3$ represents the body angular velocity vector whereas $\mathbf{p} = [e_N, e_E, e_D] \in \mathbb{R}^3$ represents the position of the aircraft in the NED frame.

Aircraft's input vector is given in Eq. 2.2 as:

$$\mathbf{u}^T = [\delta_T, \delta_{ele}, \delta_{ail}, \delta_{rud}] \in \mathbb{R}^4, \quad (2.2)$$

$$0 \leq \delta_T \leq 1, \quad (2.3)$$

$$-25^\circ \leq \delta_e \leq 25^\circ, \quad (2.4)$$

$$-21.5^\circ \leq \delta_a \leq 21.5^\circ, \quad (2.5)$$

$$-30^\circ \leq \delta_r \leq 30^\circ, \quad (2.6)$$

where δ_T , δ_e , δ_a , δ_r are the throttle position, elevator deflection, aileron deflection, and rudder deflection, respectively. Then, nonlinear aircraft dynamics can be stated in Eq. 2.7 as:

$$\dot{\mathbf{x}} = f(\mathbf{x}, \mathbf{u}). \quad (2.7)$$

Aside from all the force, moment, motion and navigational equations, state equations for angular rates are directly used in controller derivations. The state equations for angular rates are given in Eq. 2.8:

$$\begin{aligned} \dot{P} &= \frac{I_{xz}(I_{xx} - I_{yy} + I_{zz})PQ - (I_{zz}(I_{zz} - I_{yy}) + I_{xz}^2)QR + I_{zz}\sum \Delta L + I_{xz}(\sum \Delta N + Qh_x)}{I_{xx}I_{zz} - I_{xz}^2}, \\ \dot{Q} &= \frac{I_{zz} - I_{xx}PR - I_{xz}(P^2 - R^2) + \sum \Delta M - Rh_x}{I_{yy}}, \\ \dot{R} &= \frac{(I_{xx}(I_{xx} - I_{yy}) + I_{xz}^2)PQ - I_{xz}(I_{xx} - I_{yy} + I_{zz})QR + I_{xz}\sum \Delta L + I_{xx}(\sum \Delta N + Qh_x)}{I_{xx}I_{zz} - I_{xz}^2}, \end{aligned} \quad (2.8)$$

For all other detailed equations and their derivations of the HI-FI F-16 model, you may refer to [21].

2.2 Controller Derivations

2.2.1 Linear Angular Rate Regulator

Linear quadratic regulator with state feedback is employed for the angular rate regulation. Considering the relative air speed set of $S = \{200 \text{ ft/s}, 250 \text{ ft/s}, 300 \text{ ft/s}, \dots, 1000 \text{ ft/s}\}$ and the altitude set $H = \{1000 \text{ ft}, 2000 \text{ ft}, 3000 \text{ ft}, \dots, 28000 \text{ ft}\}$, the linearized forms of the Hi-Fi F-16 model, which are related to the elements of $S \times H$, are obtained while level flight conditions are assumed. Then different K vectors

are selected for each linearized model with the aid of algebraic Riccati equation [22]. During the computations of K vectors the state weighing matrix, $Q = C^T \times C$, and input weighing matrix, $R = \text{diag}(50^{-2}, 43^{-2}, 60^{-2})$, are used, where C is the output matrix of the linearized system and $\text{diag}(50^{-2}, 43^{-2}, 60^{-2})$ is representing the diagonal matrix with diagonal elements 50^{-2} , 43^{-2} , and 60^{-2} . After obtaining K vectors, lookup tables are prepared for gain scheduling in order to update the feedback gains according to varying relative air speed and altitude.

2.2.2 NDI Controller for Angular Rates

In this study a NDI controller is employed for angular rate control. As it is exhibited in Fig. 2.1, NDI controller utilizes a proportional-integral (PI) controller and inverse dynamics. PI generates the desired angular rate derivative signals. Then the desired angular rate derivations (\dot{P}_{des} , \dot{Q}_{des} , \dot{R}_{des}) together with inverse dynamics are used to compute the necessary control inputs ($\delta_{a_{cmd}}$, $\delta_{e_{cmd}}$, $\delta_{r_{cmd}}$) in order to achieve the desired angular rates.

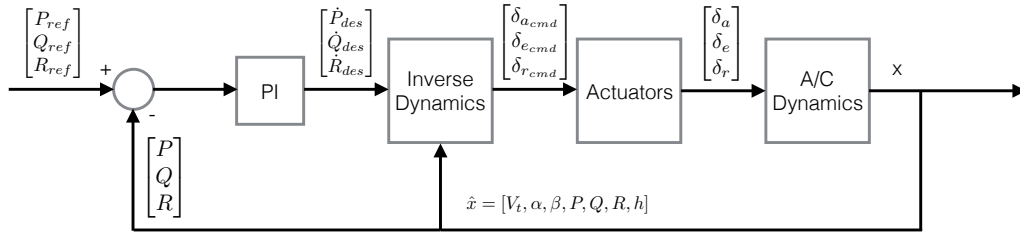


Figure 2.1 : Block diagram of NDI based angular rate controller.

In order to perform the dynamic inversion Eq. (2.8) is rearranged in the following standard form [23]:

$$\dot{x} = f(x) + g(x)u \quad (2.9)$$

where x is the state vector and u is the control input vector. Expressing the roll, pitch, and yaw moments in the following form yields:

$$\begin{aligned}
\sum \Delta L &= \bar{q}Sb[C_l(\alpha, \beta, \delta_e) + \Delta C_{l_{ief}} \delta_{ief} + \Delta C_{l_\beta} \beta + C_{l_{\delta_a}} \delta_a + C_{l_{\delta_r}} \delta_r + \frac{Rb}{2V_T} C_{lr} + \frac{Pb}{2V_T} C_{lp}] \\
\sum \Delta M &= \bar{q}S\bar{c}[C_m(\alpha, \beta, \delta_e) + \frac{Q\bar{c}}{2V_T} C_{mq} + \Delta C_m(\alpha) + \Delta C_{m_{ief}} \delta_{ief} + \\
&\quad (X_{cg_{ref}} - X_{cg})(C_z + \Delta C_{z_{ief}} \delta_{ief} + \frac{Q\bar{c}}{2V_T} C_{zq})] \\
\sum \Delta N &= \bar{q}Sb[C_n(\alpha, \beta, \delta_e) + \Delta C_{n_{ief}} \delta_{ief} + \Delta C_{n_\beta} \beta + C_{n_{\delta_a}} \delta_a + C_{n_{\delta_r}} \delta_r + \frac{Rb}{2V_T} C_{nr} + \frac{Pb}{2V_T} C_{np} - \\
&\quad (X_{cg_{ref}} - X_{cg})(C_y + \Delta C_{y_{ief}} \delta_{ief} + C_{y_{\delta_r}} \delta_r + C_{y_{\delta_a}} \delta_a + \frac{Rb}{2V_T} C_{yr} + \frac{Pb}{2V_T} C_{yp}) \frac{\bar{c}}{b}]
\end{aligned} \tag{2.10}$$

while assuming $X_{cg_{ref}} - X_{cg} = 0$. ΔC and C terms are the aerodynamic coefficients, which are all thoroughly reported in [21]. Roll and yaw moment expressions in Eq. (2.10) are appropriate for the standard form of Eq. (2.9). However, pitch moment expression is not convenient for standard form, since δ_e appears as an independent lookup table variable in $C_m(\alpha, \beta, \delta_e)$. Therefore the table inversion strategy is followed, which is explained at the end of this section.

Reorganizing the roll and yaw expressions in Eq. (2.10) yields:

$$\sum \Delta L = L_f + L_g \tag{2.11}$$

$$\sum \Delta N = N_f + N_g \tag{2.12}$$

where,

$$\begin{aligned}
L_f &= \bar{q}Sb[C_l(\alpha, \beta, \delta_e) + \Delta C_{l_{ief}} \delta_{ief} + \Delta C_{l_\beta} \beta + \frac{Rb}{2V_T} C_{lr} + \frac{Pb}{2V_T} C_{lp}] \\
N_f &= \bar{q}Sb[C_n(\alpha, \beta, \delta_e) + \Delta C_{n_{ief}} \delta_{ief} + \Delta C_{n_\beta} \beta + \frac{Rb}{2V_T} C_{nr} + \frac{Pb}{2V_T} C_{np}]
\end{aligned} \tag{2.13}$$

Note that δ_e appears also in C_l and C_n terms of Eq. (2.13) as an independent lookup table variable. Yet, the elevator is not the main control input for roll and yaw rates. In this manner, during the simulations the δ_e value of the previous time step is used while computing Eq. (2.13).

Considering f of Eq. (2.9) in the following form:

$$f(\hat{x}) = [f_P(\hat{x}) \quad f_R(\hat{x})]^T \tag{2.14}$$

where $\hat{x} = [V_T, \alpha, \beta, P, Q, R, h]^T$. Then, $f_P(\hat{x})$ and $f_R(\hat{x})$ in Eq. (2.14) can be defined as it is given in Eq. 2.15 and 2.16.

$$f_P(\hat{x}) = \frac{I_{xz}(I_{xx} - I_{yy} + I_{zz})PQ - (I_{zz}(I_{zz} - I_{yy}) + I_{xz}^2)QR + I_{zz}L_f + I_{xz}(N_f + N_T)}{I_{xx}I_{zz} - I_{xz}^2} \quad (2.15)$$

$$f_R(\hat{x}) = \frac{((I_{xx} - I_{yy})I_{xx} + I_{xz}^2)PQ - I_{xz}(I_{xx} - I_{yy} + I_{zz})QR + I_{xz}L_f + I_{xx}(N_f + N_T)}{I_{xx}I_{zz} - I_{xz}^2} \quad (2.16)$$

In addition, L_g and N_g can be computed by the following equations :

$$L_g = \bar{q}Sb(C_{l_{\delta_a}}\delta_a + C_{l_{\delta_r}}\delta_r), \quad (2.17)$$

$$N_g = \bar{q}Sb(C_{n_{\delta_a}}\delta_a + C_{n_{\delta_r}}\delta_r), \quad (2.18)$$

here, the control surface deflections δ_a and δ_r compose the control vector.

$$u = [\delta_a \quad \delta_r]^T \quad (2.19)$$

Then, the g in Eq. (2.9) will be a 2×2 matrix.

$$g(\hat{x}) = \begin{bmatrix} g_{P_a}(\hat{x}) & g_{P_r}(\hat{x}) \\ g_{R_a}(\hat{x}) & g_{R_r}(\hat{x}) \end{bmatrix} \quad (2.20)$$

where the elements of the matrix are given as follows:

$$g_{P_a}(\hat{x}) = \frac{I_{zz}\bar{q}SbC_{l_{\delta_a}} + I_{xz}\bar{q}SbC_{n_{\delta_a}}}{I_{xx}I_{zz} - I_{xz}^2} \quad (2.21)$$

$$g_{P_r}(\hat{x}) = \frac{I_{zz}\bar{q}SbC_{l_{\delta_r}} + I_{xz}\bar{q}SbC_{n_{\delta_r}}}{I_{xx}I_{zz} - I_{xz}^2} \quad (2.22)$$

$$g_{R_a}(\hat{x}) = \frac{I_{xz}\bar{q}SbC_{l_{\delta_a}} + I_{xx}\bar{q}SbC_{n_{\delta_a}}}{I_{xx}I_{zz} - I_{xz}^2} \quad (2.23)$$

$$g_{R_r}(\hat{x}) = \frac{I_{xz}\bar{q}SbC_{l_{\delta_r}} + I_{xx}\bar{q}SbC_{n_{\delta_r}}}{I_{xx}I_{zz} - I_{xz}^2} \quad (2.24)$$

Finally, the standard form for the states P and R is constructed as

$$\begin{bmatrix} \dot{P} \\ \dot{R} \end{bmatrix} = f(\hat{x}) + g(\hat{x})u \quad (2.25)$$

where f , g and u are defined above explicitly. In order to find the control surface deflections, which would produce the desired rates, the equation is inverted, assuming g is non-singular:

$$u = g(\hat{x})^{-1} \left(\begin{bmatrix} \dot{P}_{des} \\ \dot{R}_{des} \end{bmatrix} - f(\hat{x}) \right), \quad (2.26)$$

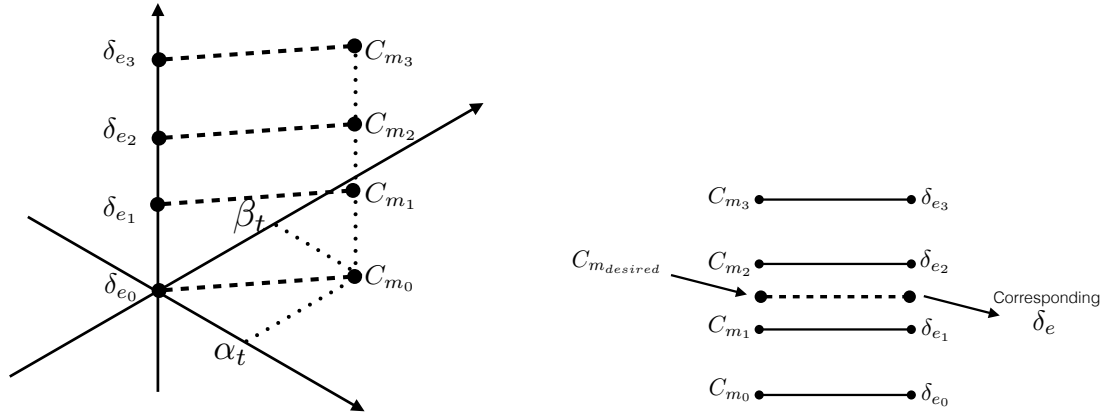
The desired pitch rate is obtained similar to roll and yaw rates as explained above. Using the desired rate, pitch rate equation is inverted to obtain desired pitch moment given as

$$M_{desired} = \dot{Q}_{des} I_{yy} - (M_T + (I_{zz} - I_{xx})PR + I_{xz}(R^2 - P^2)) \quad (2.27)$$

Similarly, using the desired moment, moment equation is inverted to obtain the C_m coefficient as follows

$$C_{m_{desired}}(\alpha, \beta, \delta_e) = \frac{M_{desired}}{\bar{q}S\bar{c}} - \left(\frac{Q\bar{c}}{2V_T} C_{mq} + \Delta C_m(\alpha) + \Delta C_{m_{lef}} \delta_{lef} \right) \quad (2.28)$$

Originally, C_m is an output of a 3-D lookup table with inputs α , β and δ_e . Considering α and β values as well as the obtained desired value for C_m at a certain time step, 2 inputs and the desired output are known. Therefore δ_e can be calculated. Lookup tables are constructed for certain amount of values for inputs and the corresponding outputs. Input points are called as breakpoints. Given the arbitrary input values, lookup tables interpolate between the existing breakpoints and calculate the output from the interpolation of the existing data points. With this information preserved, C_m values are calculated for instant α , β values and for all the available breakpoints for δ_e . Then, obtained C_m values and the breakpoints for δ_e is used to construct a 1-D lookup table. This time, desired C_m value is used as an input and the corresponding δ_e value is obtained by interpolation. This concept is illustrated in Fig. 2.2. Here, the α_t and β_t represents the values of the angle of attack and sideslip angle at the current time step.



(a) Calculation of C_m for each δ_e breakpoint at time t .

(b) Obtaining δ_e for the desired C_m .

Figure 2.2 : Description of the table inversion for elevator deflection determination.

2.2.3 NDI Controller for Angle of Attack, Sideslip and Bank Angle

NDI controller for angle of attack, sideslip and bank angle is designed using the double loop inversion technique [24]. The same double loop NDI controller is used for spin recovery in literature [13]. As it is illustrated in Fig. 2.3, double loop NDI controller consists of an inner loop PI, inner inverse laws, an outer loop PI, and outer inverse laws. All of the reference angle values are zero. Inner loop PI provides the desired angular speed rates. Then, the outer inverse laws, which is derived in this section is used to obtain reference angular rate signals. as a matter of fact, inner loop structure is exactly the same structure given in Section 2.2-2.2.2.

In the outer loop part, body axis bank angle ϕ is used instead of μ , the bank angle around velocity vector, since the state variable for μ is not modeled for the A/C model used in this paper. Rather, a nonlinear conversion is applied, via Eq. (2.29), to a reference μ angle to obtain a corresponding ϕ angle command for the controller.

$$\phi = \arccos(\cos \mu (\tan \theta \tan \alpha + 1) - \tan \theta \tan \alpha) \quad (2.29)$$

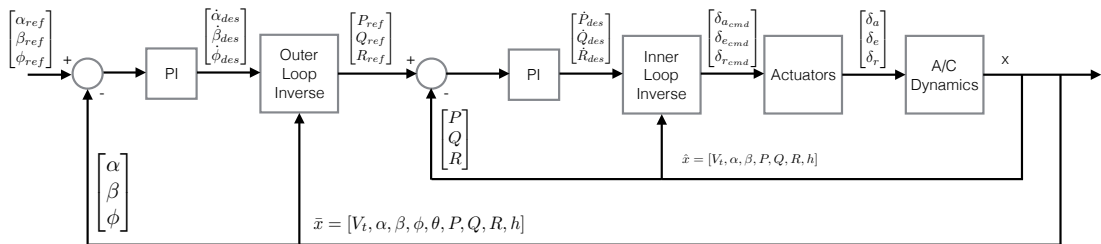


Figure 2.3 : Block diagram of the double loop NDI controller.

The outer loop inversion is carried out using the following equations for angle of attack, sideslip and bank angle.

$$\begin{aligned}
\dot{\alpha} &= Q - \tan \beta (\cos \alpha P + \sin \alpha R) + \frac{g}{V_T \cos \beta} (\cos \alpha \cos \theta \cos \phi + \sin \alpha \sin \theta) + \\
&\quad \frac{1}{mV_T \cos \beta} (A_z \cos \alpha - (A_x + T) \sin \alpha) \\
\dot{\beta} &= \sin \alpha P - \cos \alpha R + \frac{g}{V_T} (\cos \beta \cos \theta \sin \phi + \sin \beta \sin \theta \cos \alpha - \sin \alpha \sin \beta \cos \theta \cos \phi) + \\
&\quad \frac{1}{mV_T} (A_y \cos \beta - (A_x + T) \sin \beta \cos \alpha - A_z \sin \alpha \sin \beta) \\
\dot{\phi} &= P + \tan \theta (\sin \phi Q + \cos \phi R)
\end{aligned} \tag{2.30}$$

Although the forces A_x , A_y and A_z contain the inputs for control surfaces directly, their effect is negligible compare to the effects of body axis angular rates. Therefore, the body axis angular rates are considered as control inputs for the outer loop. Above equations can be partitioned to obtain the following form

$$\dot{\bar{x}} = f(\bar{x}) + g(\bar{x})v \tag{2.31}$$

where $\bar{x} = [V_t, \alpha, \beta, \phi, \theta, P, Q, R, h]^T$, $f(\bar{x}) = [f_\alpha(\bar{x}), f_\beta(\bar{x}), f_\phi(\bar{x})]^T$, and $v = [P_{cmd}, Q_{cmd}, R_{cmd}]^T$ while:

$$\begin{aligned}
f_\alpha &= + \frac{g}{V_t \cos \beta} (\cos \alpha \cos \theta \cos \phi + \sin \alpha \sin \theta) + \frac{1}{mV_t \cos \beta} (A_z \cos \alpha - (A_x + T) \sin \alpha) \\
f_\beta &= + \frac{g}{V_t} (\cos \beta \cos \theta \sin \phi + \sin \beta \sin \theta \cos \alpha - \sin \alpha \sin \beta \cos \theta \cos \phi) + \\
&\quad \frac{1}{mV_t} (A_y \cos \beta - (A_x + T) \sin \beta \cos \alpha - A_z \sin \alpha \sin \beta) \\
f_\phi &= 0
\end{aligned} \tag{2.32}$$

Then, the g in (2.31) can be represented by a 3×3 matrix

$$g(\bar{x}) = \begin{bmatrix} -\cos \alpha \tan \beta & 1 & -\sin \alpha \tan \beta \\ \sin \alpha & 0 & -\cos \alpha \\ 1 & \sin \phi \tan \theta & \cos \phi \tan \theta \end{bmatrix} \tag{2.33}$$

Finally, the v can be computed by inversion given as

$$v = g(\bar{x})^{-1}([\alpha_{des} \quad \beta_{des} \quad \phi_{des}]^T - f(\bar{x})) \quad (2.34)$$

2.2.4 Switching Controller

A switching controller, illustrated in Fig. 2.4, is proposed to control the aerodynamic angles in the presence of high angular rates. Switching controller is composed of previously explained NDI based controllers. The principal founding the switching controller is that to regulate, until a predetermined angular rate threshold is reached, the angular rates by using the controller C_1 (the NDI controller for angular rates) and then switch to C_2 (double loop NDI controller) to control the angles. Switching occurs only once from C_1 to C_2 . The angular velocity vector denoted as $\omega = [P, Q, R]^T \in \mathbb{R}^3$.

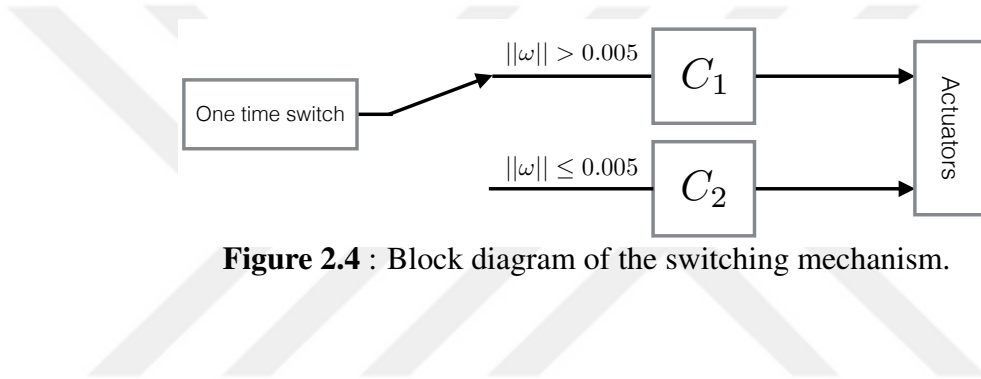


Figure 2.4 : Block diagram of the switching mechanism.

2.3 Simulation Results

Simulations are carried out in MATLAB/Simulink environment for all of the designed controllers. The aim was to obtain an envelope for angular rates such that to observe whether it is possible to recover or not when the controllers are initiated in presence of such rates. Various conditions for angle of attack are also examined. Eight different conditions for angle of attack from the set $S_0 = \{\alpha : \alpha = 4^\circ, 8^\circ, 12^\circ, 24^\circ, 36^\circ, 48^\circ, 60^\circ, 72^\circ\}$ are simulated. However, in order to keep this section plain, some of the angle of attack scenario results are not shown while the results which are sufficient to demonstrate the performance and characteristics of the controllers are present. On the other hand, the values for each element of ω is kept between -3.25 rad/s to 3.25 rad/s. Although it is not realistic for an aircraft to see such rates without risk for structural failure, the motive here is to observe the recovery abilities of the controllers in ideal conditions. In addition, it should be noted that controllers are initiated in the beginning of the simulations which are run with such initial rates. Following sections provides the plots to be seen that the controllers

Table 2.1 : Simulation stop conditions and the corresponding final simulation status.

*	Threshold	Status
$\ \omega\ $	≤ 0.005	Recovered
V_T	≥ 2000 ft/s	Unrecovered
Altitude	≤ 30 ft	Unrecovered
Load Factor	$\geq 9 \wedge \leq -3$	Unrecovered

reduce the rates to acceptable values rapidly such that the aircraft is not exposed to unnatural high rates for considerable amount of time. The condition for recovery is set as $\|\omega\| = \sqrt{(P_{ref} - P)^2 + (Q_{ref} - Q)^2 + (R_{ref} - R)^2} \leq 0.005$.

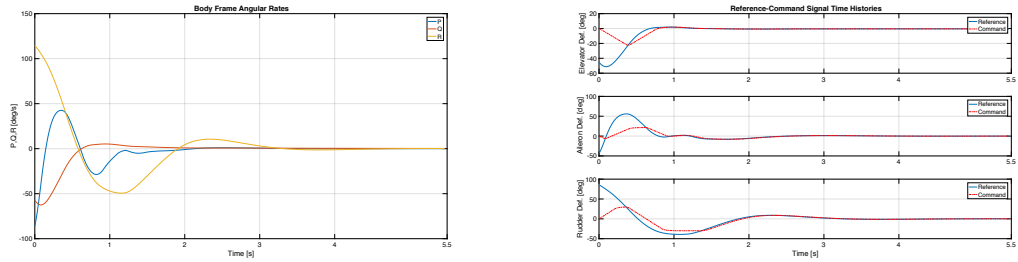
Furthermore, simulations are supported with stop conditions on altitude, total velocity and load factor. If the aircraft is out of the limits for these parameters, which are given in Table 2.1, the simulation is stopped and that node is considered as unrecovered. Therefore, it is made sure that the aircraft stays in certain limits to be considered as recovered. In following sections, the colors in envelope plots represents the time of recovery of that node such that green, black and blue represents recovery under 8, 15, and 100 seconds respectively whereas red color represents failed recovery attempt. Simulations are limited to 100 seconds for computational restrictions. Therefore, recovery attempts which would take more than 100 seconds are considered failed recoveries. In subsequent sections, detailed results are presented while giving out discussions on thought-provoking observations.

2.3.1 Linear Controller

First, linear controller is tested to regulate the angular rates. Simulations are run for initial angular rates ranging in the interval $[-3, 3]$ radian/s with the increments of 0.5 radian. Total of 2197 ω values are used as a starting node to simulations for each initial angle of attack value from the set $S_1 = \{\alpha : \alpha = 4^\circ, 8^\circ, 12^\circ, 24^\circ\}$. Simulations are kept in a narrow set for angle of attack and partial set for ω compare to the simulation runs for nonlinear controllers. The reason is the fact that linear controllers are effective around lower angle of attacks so that the reduced amount of simulations are seen sufficient to show the performance of this controller and ω envelope.

To begin with, one of the successfully recovered case result is shown in Figs 2.5 and 2.6. Initially, the angle of attack is 12° and $\omega = [-1.5, -1, 2]$. Rates are rapidly

reduced to much lower values in under a second as it is mentioned earlier. Control input are saturated in transient part. However, saturation is lagged since the actuators are modeled with rate limiters.



(a) Angular rate time history.

(b) Reference-command input time history.

Figure 2.5 : Angular rate and reference-command input time history results obtained from the simulations where LQR is employed for the angular rate regulation. Initial roll rate, pitch rate, yaw rate, and angle of attack are -1.5 rad/s , -1 rad/s , 2 rad/s and 12° , respectively.

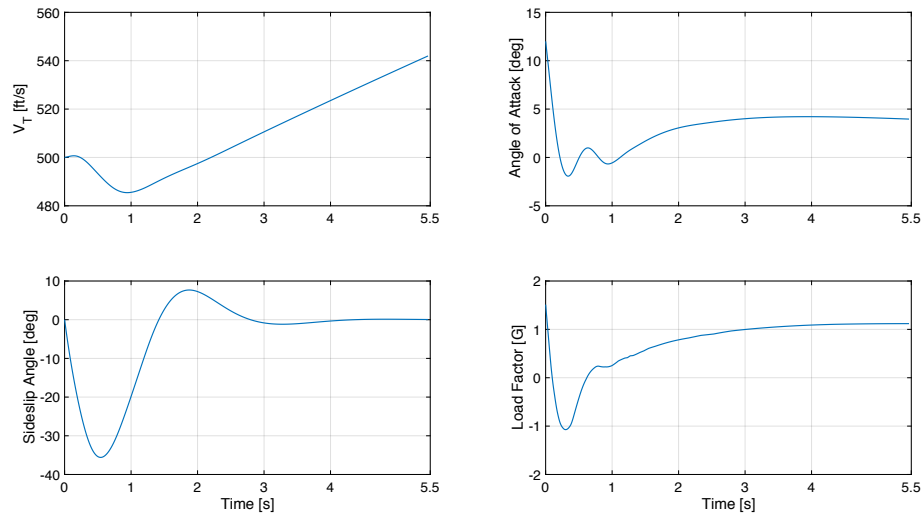
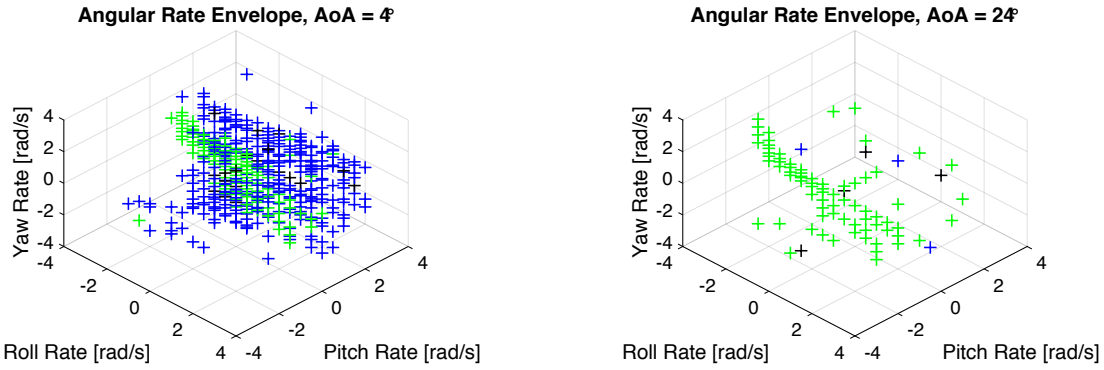


Figure 2.6 : Relative airspeed, angle of attack, sideslip angle, and load factor time histories obtained from the simulations where LQR is employed for the angular rate regulation.

Fig. 2.7 demonstrate the ω envelopes.

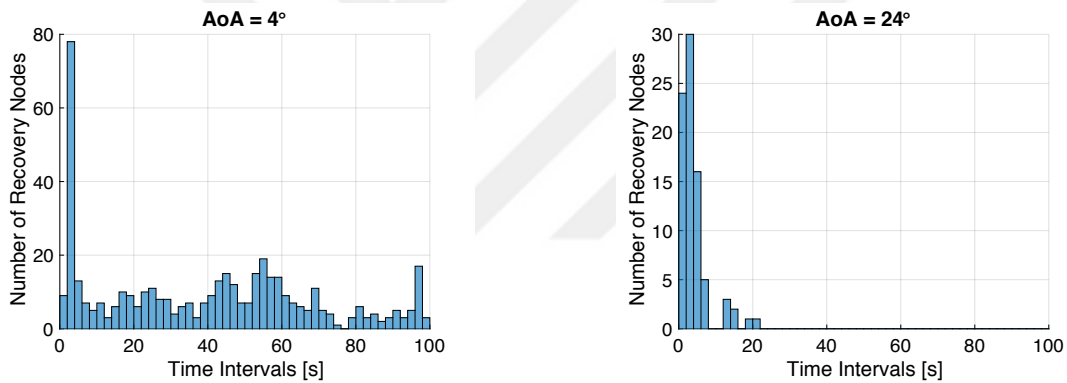


(a) 4° initial angle of attack case, nodes where regulation is achieved.

(b) 24° initial angle of attack case, nodes where regulation is achieved.

Figure 2.7 : The angular rate envelopes obtained for the linear quadratic regulator while considering 4° and 24° initial angle of attack scenarios: Green nodes represents (0-8)s regulation time, black nodes represents (8-15)s regulation time, and blue nodes represents (15-100)s regulation time.

Histograms of the same cases can be seen in Fig. 2.8.



(a) 4° angle of attack case, number of recovery nodes vs. regulation time interval histogram.

(b) 24° angle of attack case, number of recovery nodes vs. regulation time interval histogram.

Figure 2.8 : The number of regulation nodes vs. regulation time interval histograms obtained for the linear quadratic regulator while considering 4° and 24° initial angle of attack scenarios

Based on these results, it can be stated that linear controller is indeed successful in a limited region. Envelope plots also demonstrate that recoverable region is shrinking if the initial angle of attack gets higher. This result can be further seen in Fig. 2.29 at the end of this section. Nonetheless, linear controller has unforeseen performance on recovery time. Histograms in Figs 2.8 show that recovery process is significantly rapid for most of the recovered nodes.

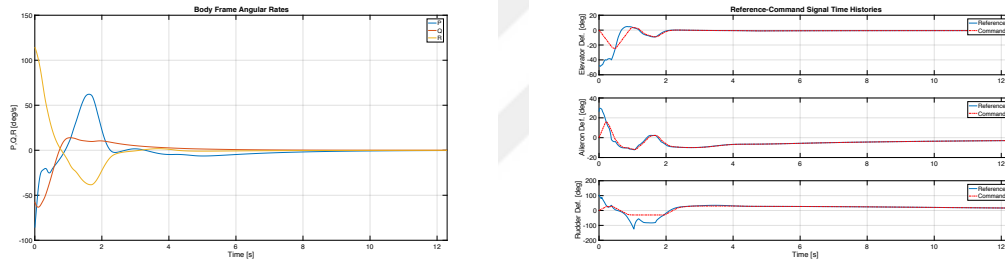
Despite its good performance on recovery time, linear controller's ω envelope is restricted to small region and the effectiveness of the controller is decreasing with

increase in angle of attack. However, for agile maneuvering aircrafts, high angles of attack and high angular rates are inevitable. Therefore, nonlinear controllers are necessary in order to capture the dynamics in harsh conditions.

2.3.2 Single Loop NDI Controller (C_1)

In order to observe the metrics extensively, simulations are run for two sets of ω . In addition to interval $[-3,3]$ radian, nodes are also selected from the interval $[-3.25,3.25]$ with increment of 0.5 radian which makes total of 4941 nodes. Remind that simulations are run for all these initial ω 's at each initial angle of attack values from the set S_0 .

Single case for C_1 is selected with same conditions as the single case for linear controller. It is seen from Figures 2.9-2.10 that inputs are saturated for longer periods compare to linear controller whereas the loading on aircraft is less.



(a) Angular rate time history.

(b) Reference-command input time history.

Figure 2.9 : Angular rate and reference-command input time history results obtained from the simulations where C_1 is employed for the angular rate regulation. Initial roll rate, pitch rate, yaw rate, and angle of attack are -1.5 rad/s, -1 rad/s, 2 rad/s and 12° , respectively.

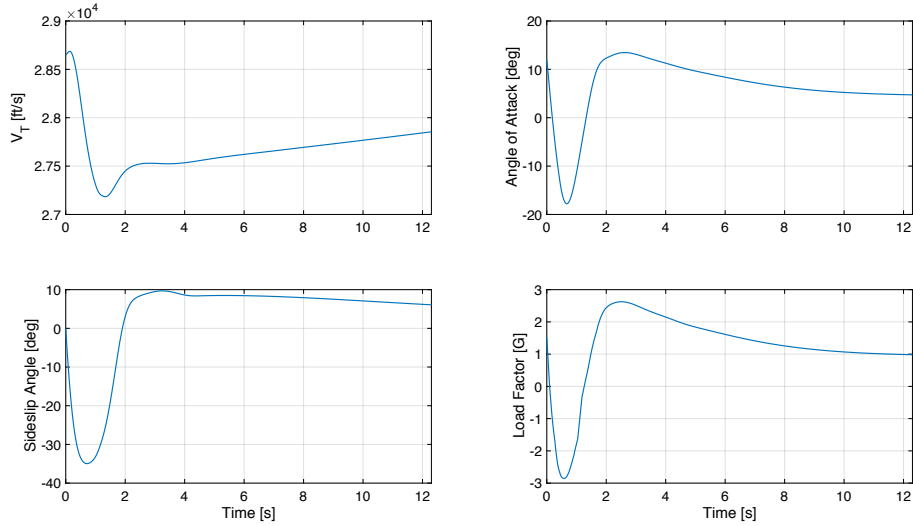


Figure 2.10 : Relative airspeed, angle of attack, sideslip angle, and load factor time histories obtained from the simulations where C_1 is employed for the angular rate regulation.

Single run sample for C_1 controller is given in Fig. 2.11.

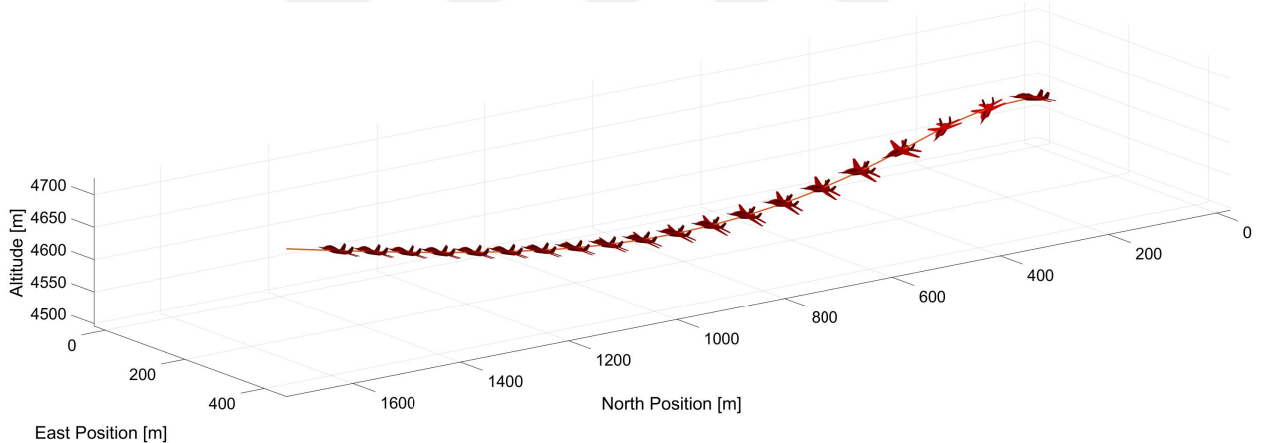
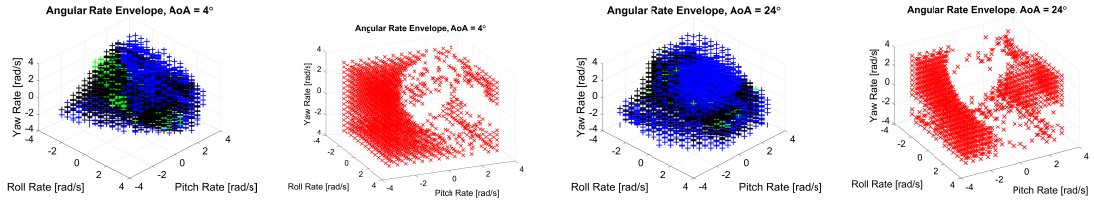


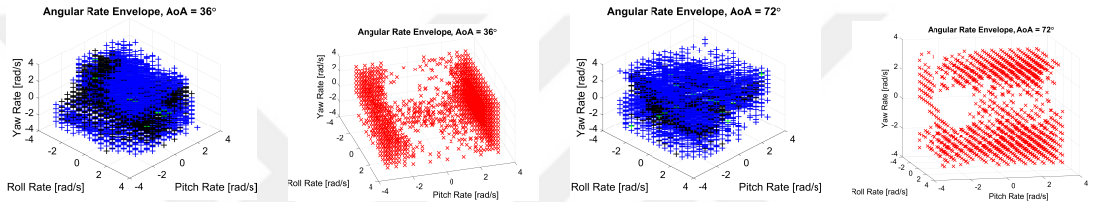
Figure 2.11 : Flight trajectory obtained from the simulations where C_1 is employed for the angular rate regulation.

ω envelope for C_1 controller is given in Figs 2.12-2.13. Similar to the results in linear controller, pitch rate is the most effective cause on recoverability due to load factor limitations. Comparing to linear controller, there is an undeniable grow in the recoverable region. At $\alpha = 36^\circ$, pitch rate is still the most critical factor for recoverability which can be seen in figure 2.13. However, yaw rate is getting more effective for recoverability if angle of attack is further increased as it can be seen from Fig. 2.13.



(a) 4° initial angle of attack case, nodes where regulation is achieved. (b) 4° initial angle of attack case, nodes where regulation is failed. (c) 24° initial angle of attack case, nodes where regulation is achieved. (d) 24° initial angle of attack case, nodes where regulation is failed.

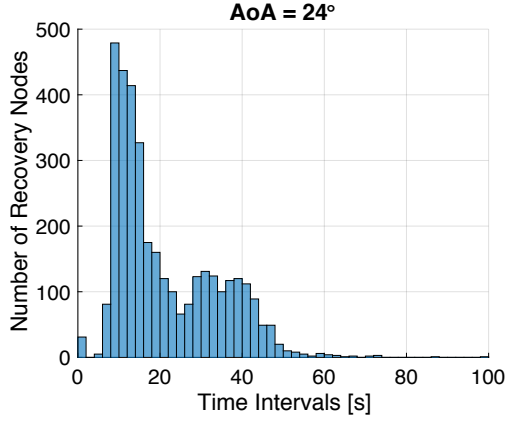
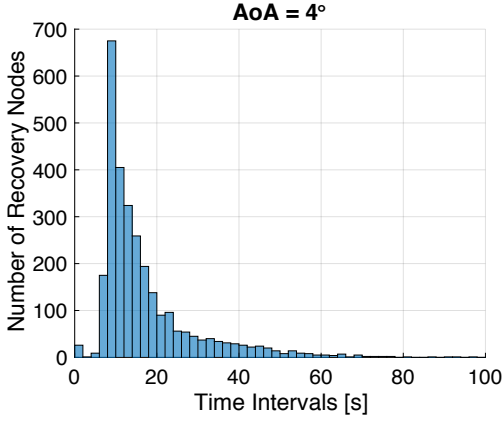
Figure 2.12 : The angular rate envelopes obtained for C_1 while considering 4° and 24° initial angle of attack scenarios: Green nodes represents (0-8)s regulation time, black nodes represents (8-15)s regulation time, blue nodes represents (15-100)s regulation time and red nodes represents regulation fails.



(a) 36° initial angle of attack case, nodes where regulation is achieved. (b) 36° initial angle of attack case, nodes where regulation is failed. (c) 72° initial angle of attack case, nodes where regulation is achieved. (d) 72° initial angle of attack case, nodes where regulation is failed.

Figure 2.13 : The angular rate envelopes obtained for C_1 while considering 36° and 72° initial angle of attack scenarios: Green nodes represents (0-8)s regulation time, black nodes represents (8-15)s regulation time, blue nodes represents (15-100)s regulation time and red nodes represents regulation fails.

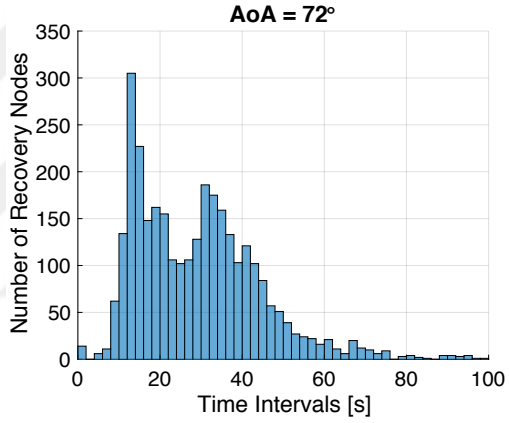
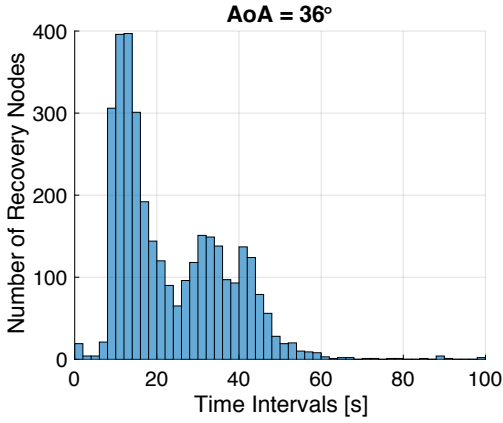
The results in figures 2.14-2.15 show that the recovery times shift to the longer time periods with increasing angle of attack.



(a) 4° angle of attack case, number of recovery nodes vs. regulation time interval histogram.

(b) 24° angle of attack case, number of recovery nodes vs. regulation time interval histogram.

Figure 2.14 : The number of regulation nodes vs. regulation time interval histograms obtained for C_1 while considering 4° and 24° initial angle of attack scenarios.



(a) 36° angle of attack case, number of recovery nodes vs. regulation time interval histogram.

(b) 72° angle of attack case, number of recovery nodes vs. regulation time interval histogram.

Figure 2.15 : The number of regulation nodes vs. regulation time interval histograms obtained for C_1 while considering 36° and 72° initial angle of attack scenarios.

It is clear that controller C_1 has a satisfactory performance for regulation of the angular rates. However, there can be situations that the controller is terminated due to completion of regulation of ω whereas the terminal angle of attack is in a dangerous region for regular flight controls or a pilot of the aircraft. For this reason, the controller C_2 is implemented to use for recovery while controlling the angle of attack.

2.3.3 Double Loop NDI Controller (C_2)

Simulations are run for the same conditions as it is done for previous controller. Distinctively, the condition for a successful recovery is enlarged such that $\|\alpha, \beta, \phi\| \leq$

0.005 and $\|\omega\| \leq 0.005$ need to be satisfied at the same time, where

$$\|[\alpha, \beta, \phi]\| = \sqrt{(\alpha_{ref} - \alpha)^2 + (\beta_{ref} - \beta)^2 + (\phi_{ref} - \phi)^2}$$

Single case for C_2 controller is chosen with initial condition $\omega = [1.75, -0.75, 0.75]$ and $\alpha = 12^\circ$. The results for state and input histories are given in Figs. 2.16-2.18.

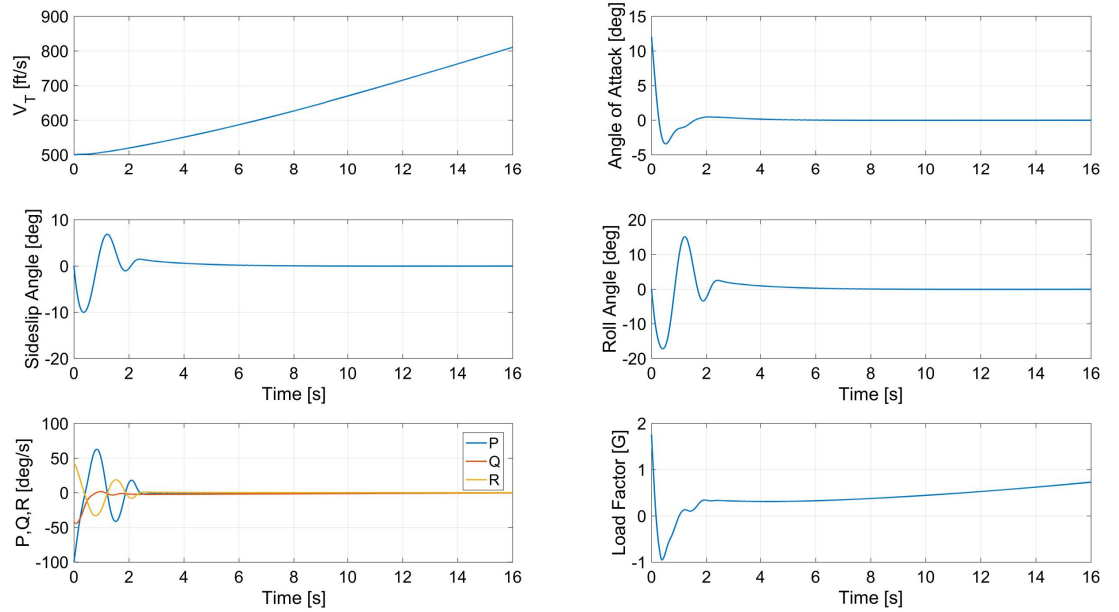


Figure 2.16 : Relative airspeed, angle of attack, sideslip angle, angular rate, and load factor time histories obtained from the simulations where C_2 is employed. Initial roll rate, pitch rate, yaw rate, and angle of attack are 1.75 rad/s, -0.75 rad/s, 0.75 rad/s and 12° , respectively.

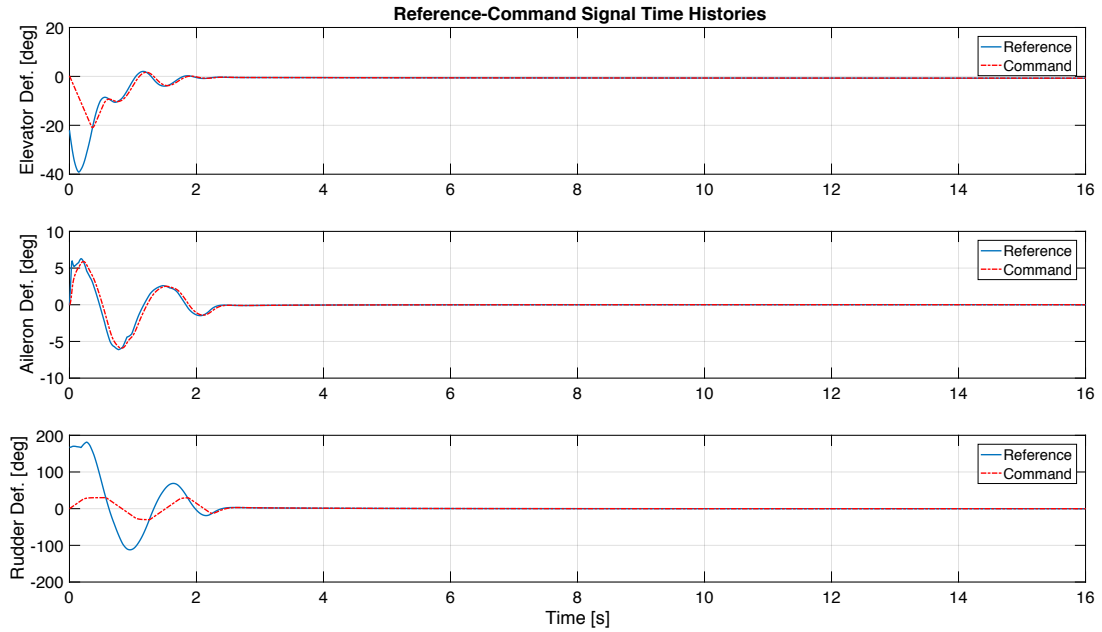


Figure 2.17 : Reference-command input time history results obtained from the simulations where C_2 is employed. Initial roll rate, pitch rate, yaw rate, and angle of attack are 1.75 rad/s, -0.75 rad/s, 0.75 rad/s and 12° , respectively.

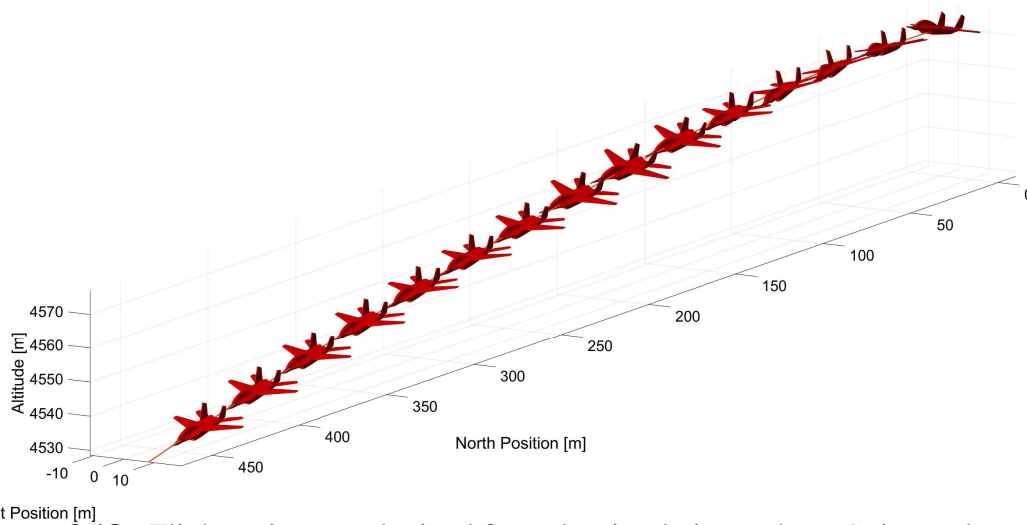
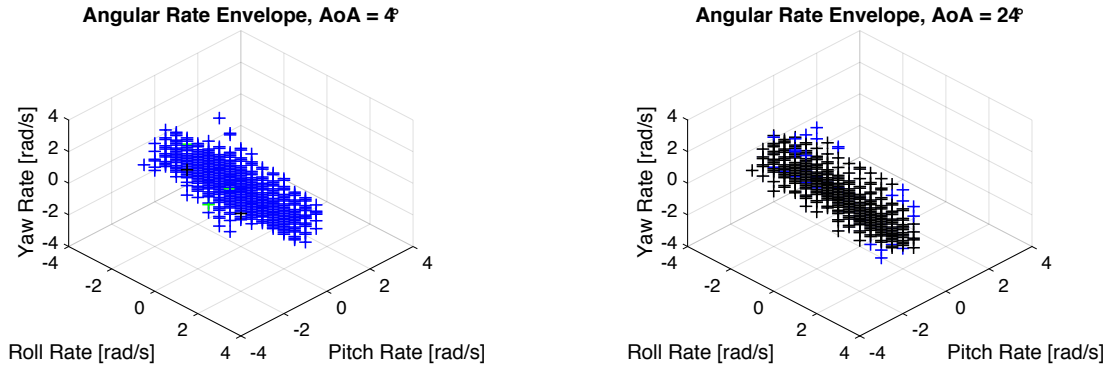


Figure 2.18 : Flight trajectory obtained from the simulations where C_2 is employed for the angular rate regulation.

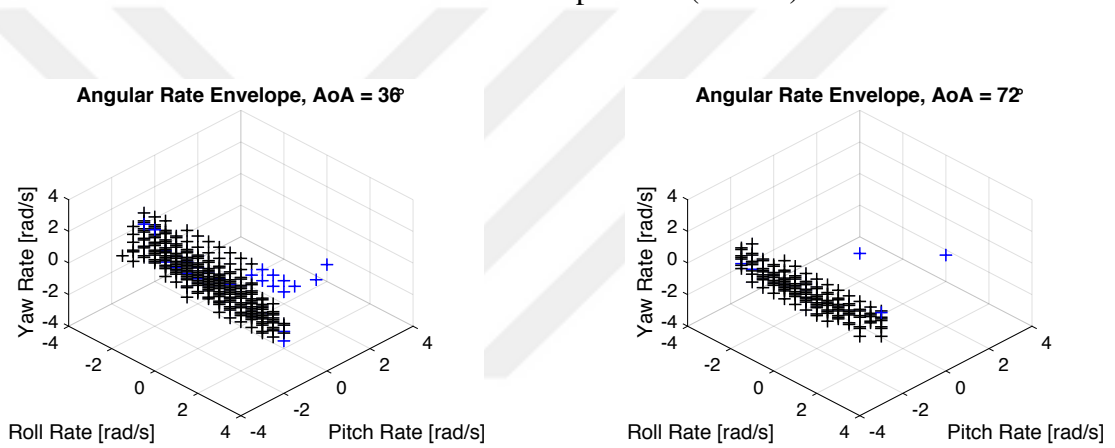
ω envelopes in Figs. 2.19-2.20 presents that C_2 controller is successful in a quite restricted region. Envelope plots clearly demonstrate that high pitch and yaw rates limit ability to control aerodynamic angles.



(a) 4° initial angle of attack case, nodes where recovery is achieved.

(b) 24° initial angle of attack case, nodes where recovery is achieved.

Figure 2.19 : The angular rate envelopes obtained for C_2 while considering 4° and 24° initial angle of attack scenarios: Green nodes represents (0-8)s regulation time, black nodes represents (8-15)s recovery time, and blue nodes represents (15-100)s.



(a) 36° initial angle of attack case, nodes where recovery is achieved.

(b) 72° initial angle of attack case, nodes where recovery is achieved.

Figure 2.20 : The angular rate envelopes obtained for C_2 while considering 36° and 72° initial angle of attack scenarios: Green nodes represents (0-8)s regulation time, black nodes represents (8-15)s recovery time, and blue nodes represents (15-100)s.

The results show that recovery performance of controller C_2 is poor compared to C_1 . Yet, function of the controller C_2 can not be abandoned. Despite the fact that regulation of angular rates has the priority to regain control of agile maneuvering aircraft, recovering the aerodynamic angles are also significant. Because the possibility to re-entering a control loss situation is not vanished. In order to take the advantage of C_1 's ability to regulate angular rates, a new control method is proposed by making use of both C_1 and C_2 controllers which can be named as *Switching NDI Controller*.

The aim of this proposition is to enlarge the recoverability region while controlling the aerodynamic angles.

2.3.4 Switching NDI Controller (C_3)

The idea to elevate the performance of C_2 by combining it with C_1 is tested in these set of simulations. Again, the same initial conditions are applied to be able to make clear comparisons. Switching condition is taken as $\|\omega\| \leq 0.005$ whereas the condition for successful recovery is set same with the case in C_2 controller.

Motivation to use this controller over single loop NDI controller(C_1) is demonstrated in Fig. 2.21 unambiguously. Here, the single loop NDI controller terminates, regulates the body axis angular rates, prior to red line shown. It can be seen that the aircraft has a slight sideslip angle and a significant bank angle. Although the C_1 controller has done its duty, it is clearly not safe to leave the aircraft in such condition. Fortunately, C_3 controller is able to switch at that point, where the red line is, to continue recovery process and successfully regulates the aerodynamic angles.

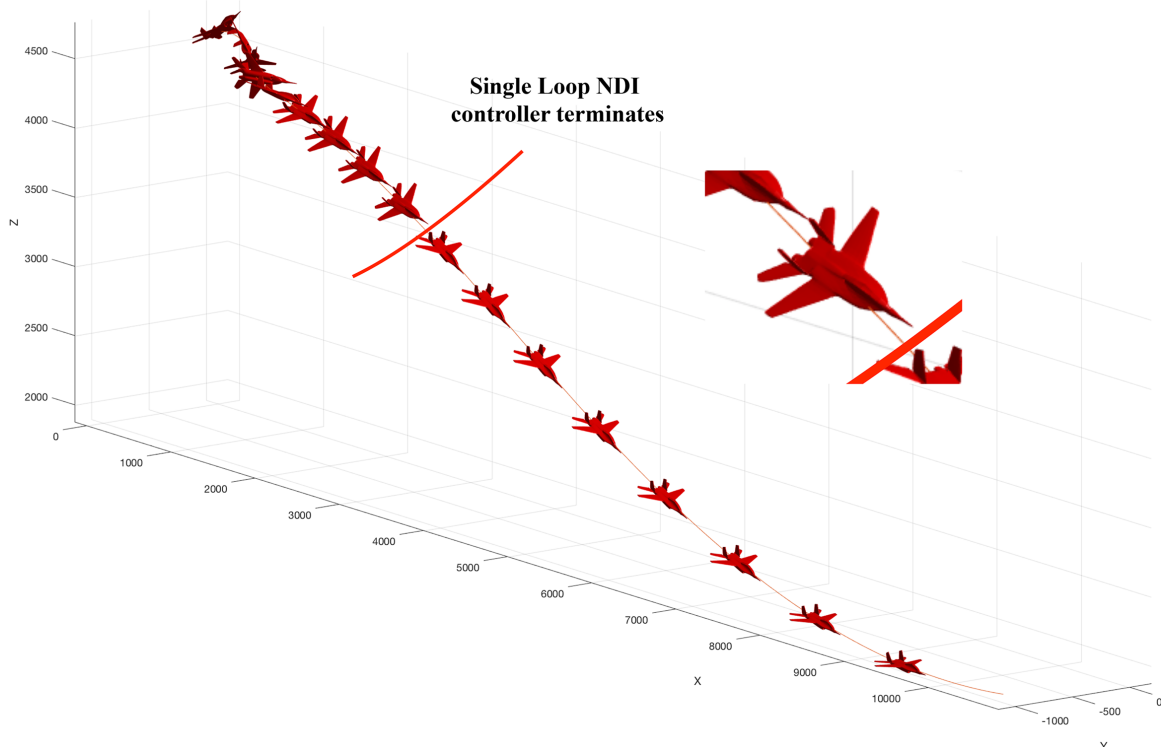


Figure 2.21 : Trajectory plot for C_3 . Initial angle of attack is 36° and $\omega = [1, 0.5, -3]^T$

Single case for switching controller is chosen with initial conditions identical to the case for C_2 controller. Switching occurs where the sudden changes in signals take place that can be seen in Figs. 2.22, 2.23 and 2.24

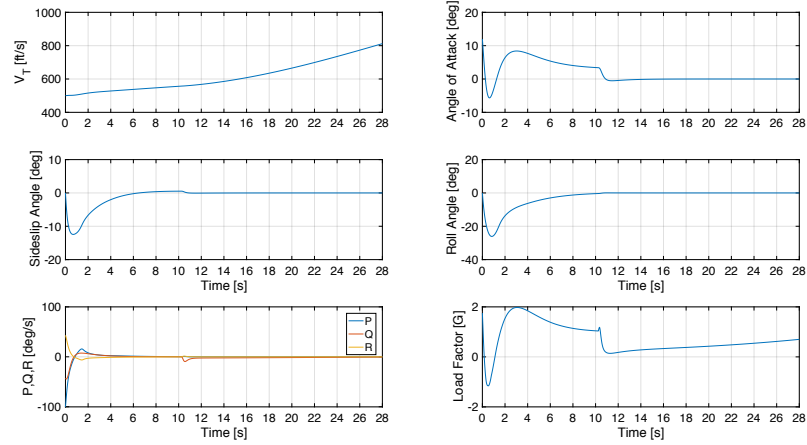


Figure 2.22 : Relative airspeed, angle of attack, sideslip angle, angular rate, and load factor time histories obtained from the simulations where C_3 is employed. Initial roll rate, pitch rate, yaw rate, and angle of attack are 1.75 rad/s, -0.75 rad/s, 0.75 rad/s and 12° , respectively.

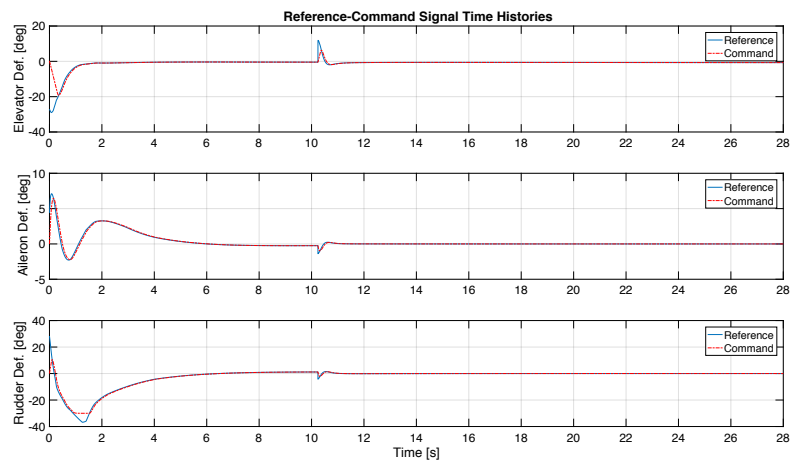


Figure 2.23 : Reference-command input time history results obtained from the simulations where C_3 is employed. Initial roll rate, pitch rate, yaw rate, and angle of attack are 1.75 rad/s, -0.75 rad/s, 0.75 rad/s and 12° , respectively.

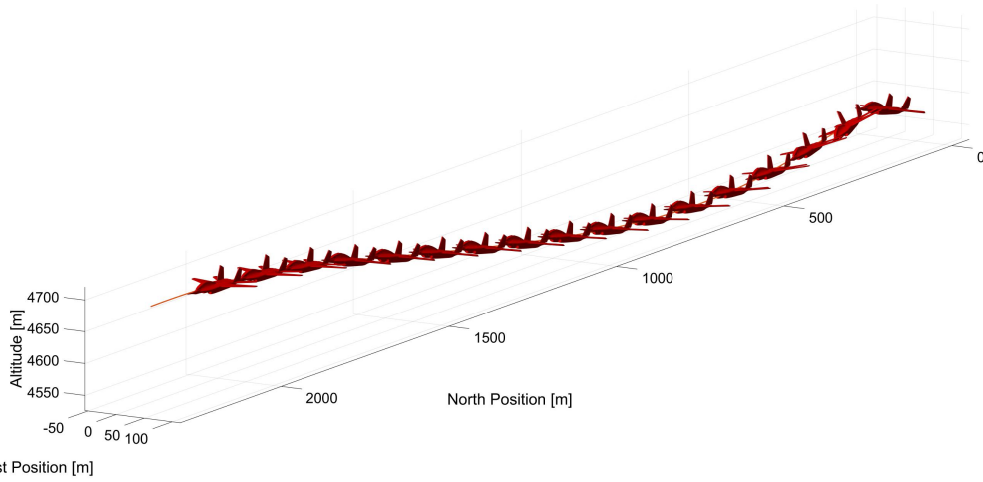
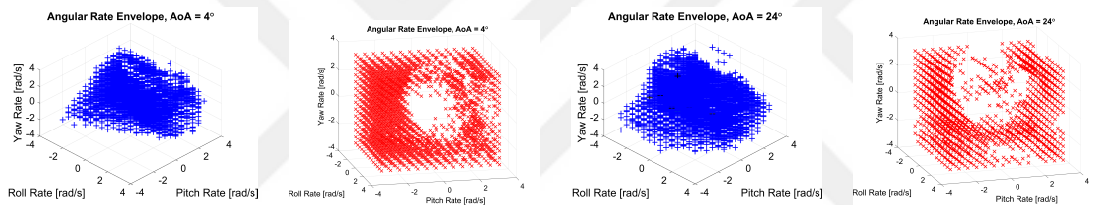


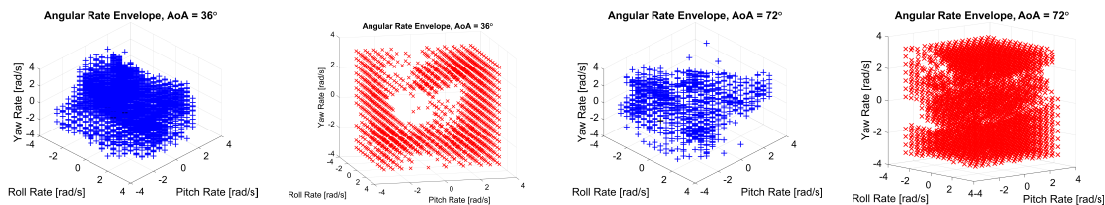
Figure 2.24 : Flight trajectory obtained from the simulations where C_3 is employed for the angular rate regulation.

Proposed method has indeed enlarged the ω envelope significantly which can be seen in Figs. 2.25-2.26.



(a) 4° initial angle of attack case, nodes where recovery is achieved. (b) 4° initial angle of attack case, nodes where recovery is failed. (c) 24° initial angle of attack case, nodes where recovery is achieved. (d) 24° initial angle of attack case, nodes where recovery is failed.

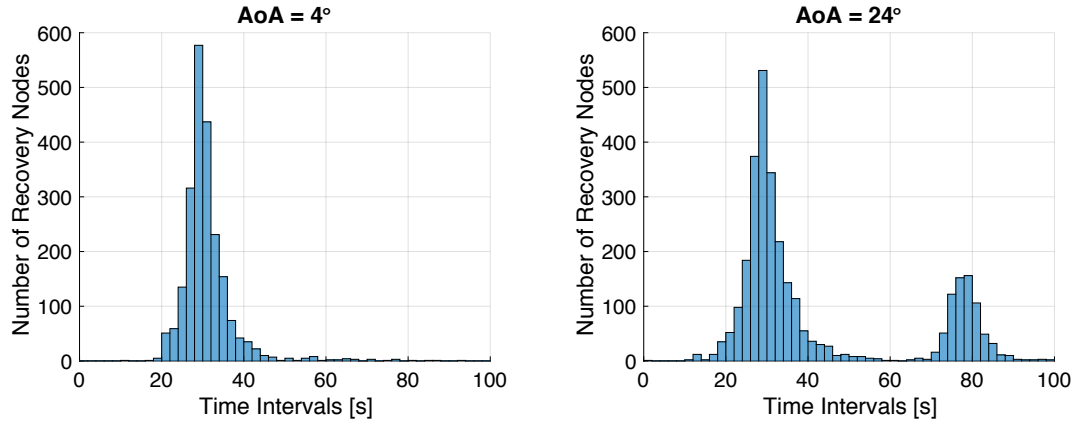
Figure 2.25 : The angular rate envelopes obtained for C_3 while considering 4° and 24° initial angle of attack scenarios: Green nodes represents (0-8)s recovery time, black nodes represents (8-15)s recovery time, blue nodes represents (15-100)s recovery time and red nodes represents recovery fails.



(a) 36° initial angle of attack case, nodes where recovery is achieved. (b) 36° initial angle of attack case, nodes where recovery is failed. (c) 72° initial angle of attack case, nodes where recovery is achieved. (d) 72° initial angle of attack case, nodes where recovery is failed.

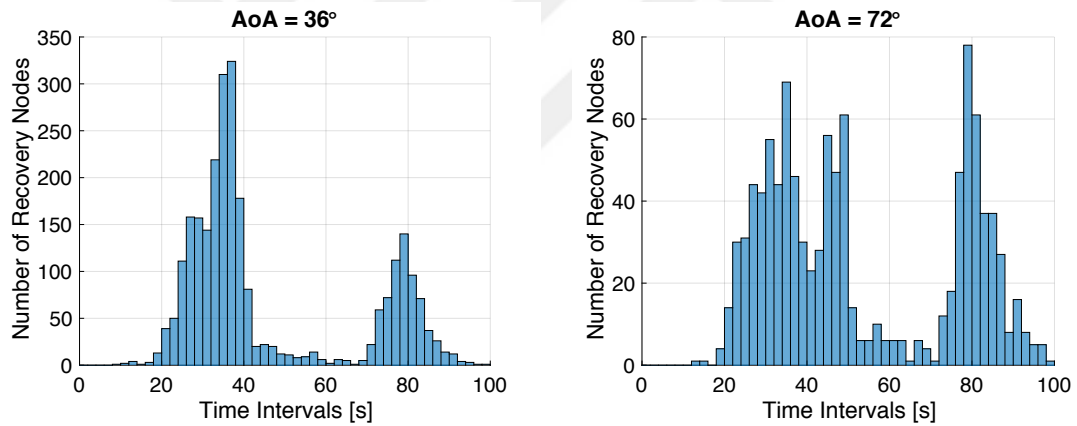
Figure 2.26 : The angular rate envelopes obtained for C_3 while considering 36° and 72° initial angle of attack scenarios: Green nodes represents (0-8)s recovery time, black nodes represents (8-15)s recovery time, blue nodes represents (15-100)s recovery time and red nodes represents recovery fails.

Histograms in Figures 2.27-2.28 shows that recovery times creates a bimodal graphs as the angle of attack increases.



(a) 4° angle of attack case, number of recovery nodes vs. recovery time interval histogram. (b) 24° angle of attack case, number of recovery nodes vs. recovery time interval histogram.

Figure 2.27 : The number of recovery nodes vs. recovery time interval histograms obtained for C_3 while considering 4° and 24° initial angle of attack scenarios.



(a) 36° angle of attack case, number of recovery nodes vs. recovery time interval histogram. (b) 72° angle of attack case, number of recovery nodes vs. recovery time interval histogram.

Figure 2.28 : The number of recovery nodes vs. recovery time interval histograms obtained for C_3 while considering 36° and 72° initial angle of attack scenarios.

The motive in switching controller was to make the regulation of angular rates prior to control of angles. In all simulations, regulation is considered successful if $\|\omega\| \leq 0.005$ is satisfied. Therefore, the switch condition is set according to this motive. However, the requirements for successful recovery in these simulations already contains the regulation of rates according to given threshold. Hence, there is no dependence to pick the switch condition same as the terminal conditions. In addition to that, it is observed in the simulation results that controller takes considerable amount of

time to make small corrections so that switching can occur. To save that time, relaxing the threshold for switching is experimented with further simulations. This time the switch condition is set as $\|\omega\| \leq 0.02$.

When the whole region is concerned, changing the switch condition has indeed reduced the recovery times as it can be later seen in Fig. 2.32.

Finally, the recovery performance of the all controllers are compared in Figs. 2.29 and 2.30. According to Fig. 2.29, single loop angular rate controller(C_1) has better performance compare to linear controller and linear controller has poor performance as the angle of attack increases. Double loop NDI controller(C_2) has shown poor performance that is close to the performance of linear controller. On the other hand, switching controller with and without relaxed switch, has shown promising performance. It would be better to remind that, although the number of recovered nodes is not separated significantly, relaxing the switch has shown improvement on the recovery times as it is seen in Fig. 2.32 which was its main purpose.

Another intriguing observation derived from Figs. 2.29 and 2.30 is that the number of recovery nodes versus the angle of attack curves of the nonlinear angular rate controller and the switching controller resembles the lift coefficient curve with respect to angle of attack $C_{L\alpha}$ which is given in figure 2.31.

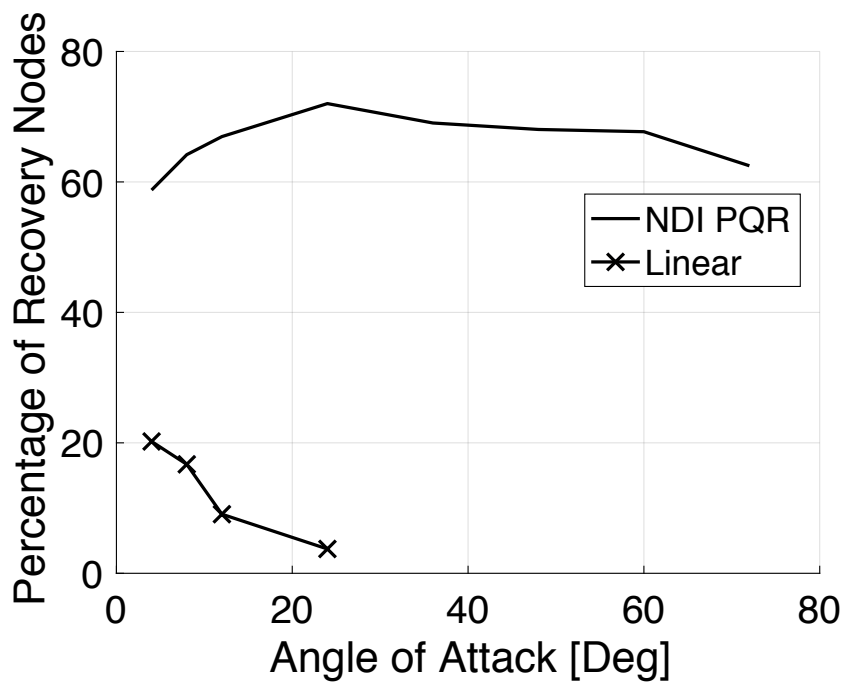


Figure 2.29 : Percentage of recovery nodes vs. angle of attack graph of linear and C_1 (NDI PQR) controllers.

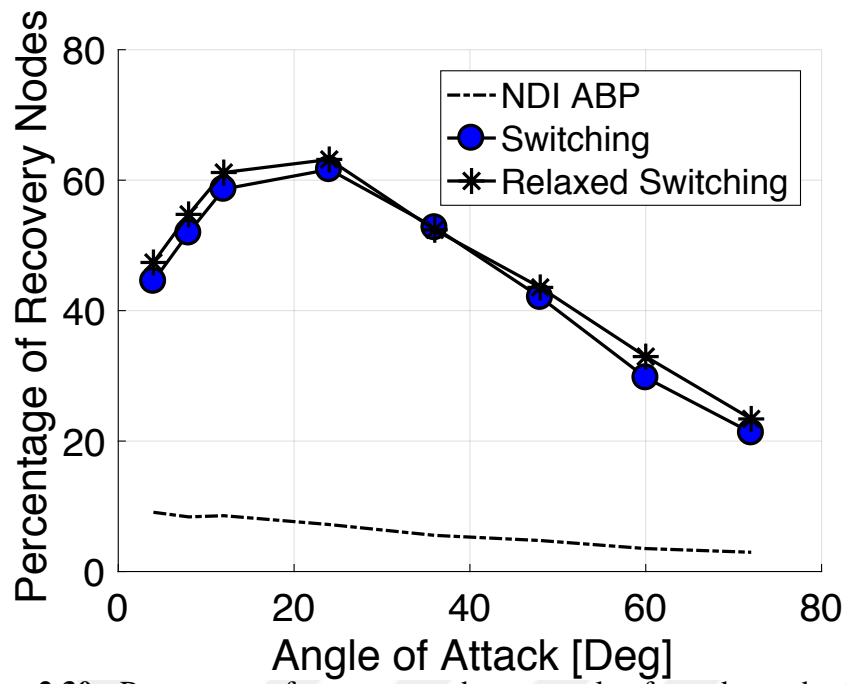


Figure 2.30 : Percentage of recovery nodes vs. angle of attack graph of C_2 (NDI ABP), C_3 (switching), and C_4 (relaxed switching) controllers.

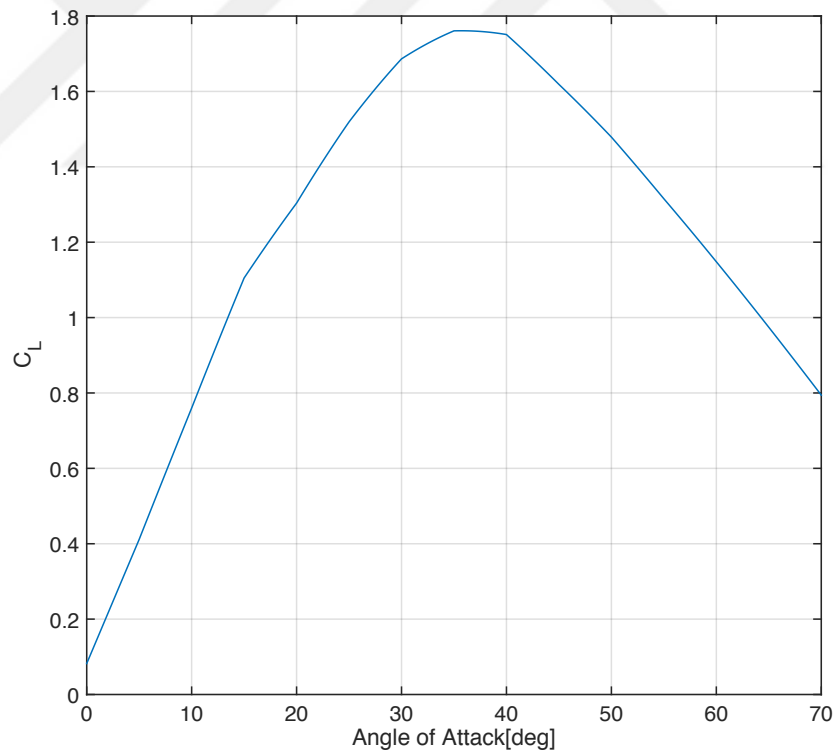


Figure 2.31 : Lift coefficient distribution with respect to angle of attack, where $\delta_e = 0$. This curve is obtained from the aerodynamic database of the Hi-Fi F-16 model in this study.

Aforementioned recovery time results are given in Fig. 2.32.

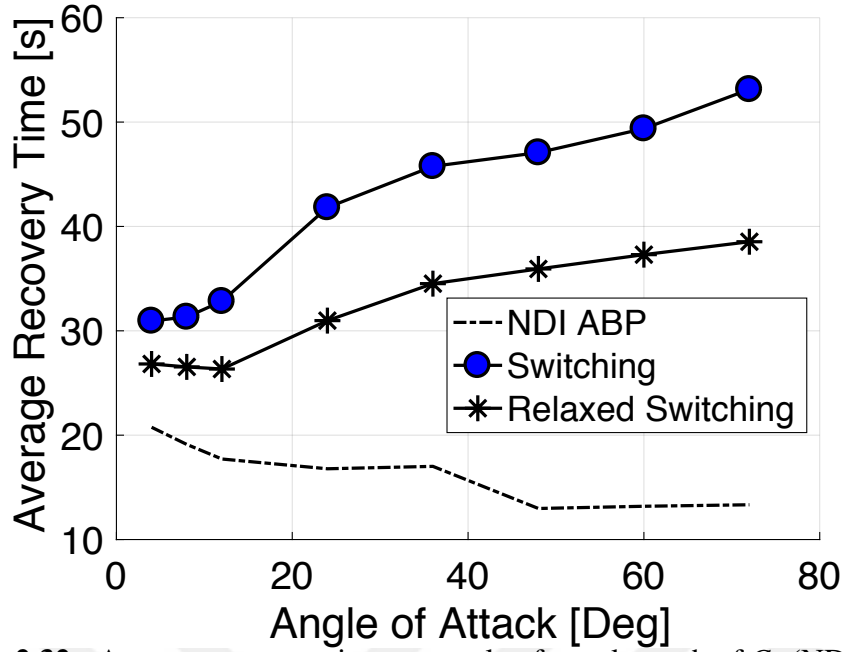


Figure 2.32 : Average recovery time vs. angle of attack graph of C_2 (NDI ABP), C_3 (switching), and C_4 (relaxed switching) controllers.

2.4 Middle State Approach

In order to optimize the regulation time, a search is made to explore an intermediate state that would minimize time to reach origin state ($[P, Q, R] = [0, 0, 0]$). Due to computational limits, restricted space is explored and only one intermediate state is searched. Three components of the starting points on the space is selected from sets

$$P = [-0.5, -0.25, 0, 0.25, 0.5] \quad Q = [-0.5, 0, 0.5] \quad R = [-1.5, -1, -0.5, 0, 0.5, 1, 1.5] \quad (2.35)$$

For each starting point, first reference signals are selected from same sets that construct the space which is investigated. If the aircraft reaches the first reference state, origin point is given as a second reference signal. The condition to reach the reference state is selected as $\|\omega\| < 0.005$. Reference switching is illustrated in Fig. 2.33

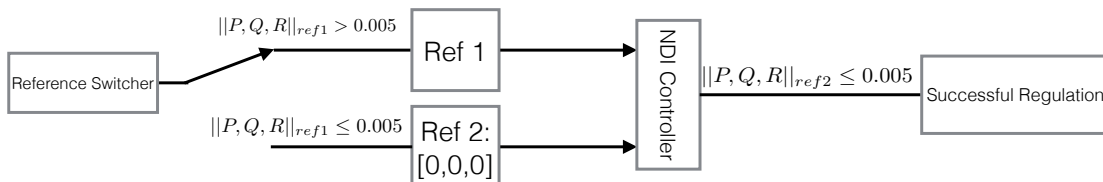


Figure 2.33 : Illustration of reference generation

Monte Carlo simulations are carried out using the strategy explained above. Total of 105 starting points are guided to origin using $105^2 = 11025$ paths. Each starting point

is taken to origin from 105 different paths including direct path(no intermediate state) to origin. Note that other paths include only one intermediate state. All paths are stored with informations of intermediate states, success in regulation and total regulation time. Using this information, minimum time paths are determined using bubble sort algorithm. Unsuccessful regulations are eliminated as well as the trivial solutions which are direct paths to origin. The other solutions which contains intermediate states are presented in Fig. 2.34. The letters A,B, and O represent the starting points, intermediate states and origin respectively.

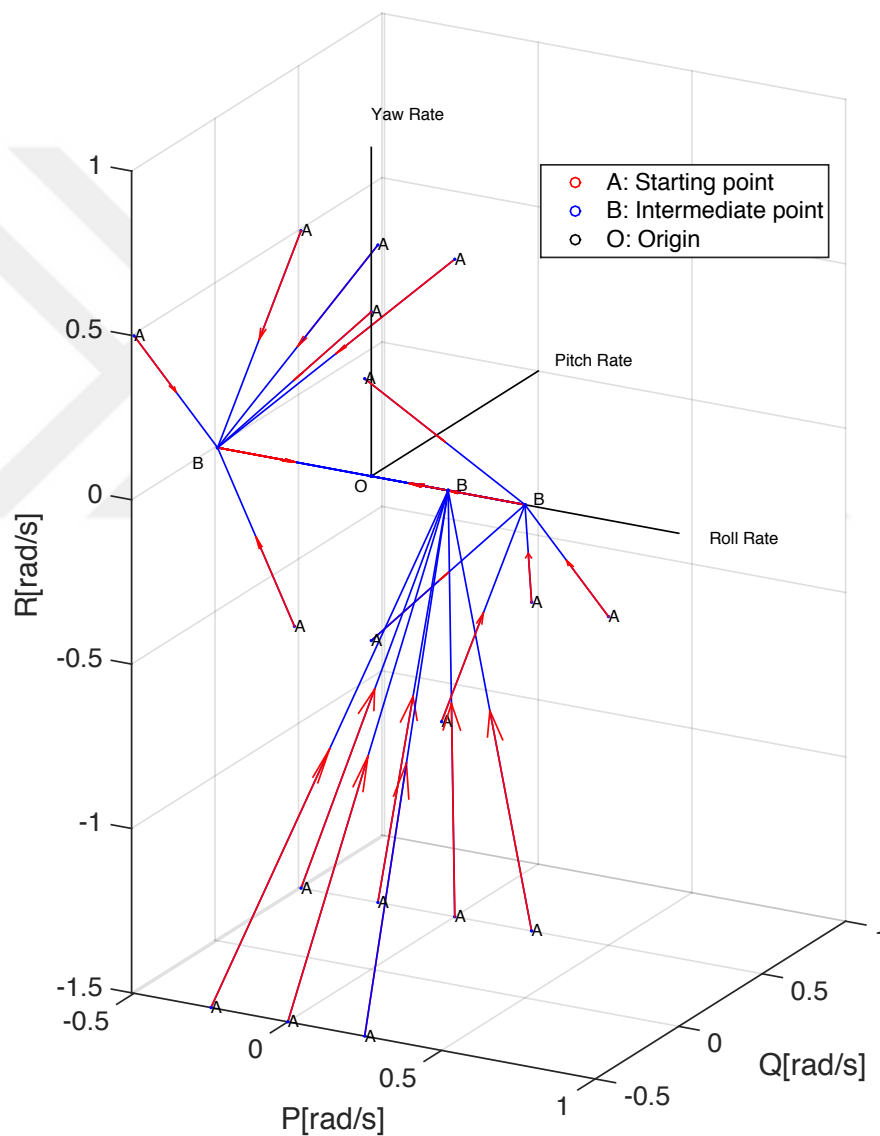


Figure 2.34 : Optimal time paths for regulation of angular rates

It can be noticed that all the intermediate states are on the roll rate axis. The aircraft is not stable with existence of pitch and yaw rates. On the other hand, the

recommendation can be made in some cases such that it is beneficial to roll preliminary to regulate the angular rates in terms of time.



3. NEURAL NETWORK APPROACH FOR RECOVERABILITY ENVELOPE ESTIMATION

In this chapter, neural network approach is implemented to classify the states properly in order to estimate recoverability envelope using the previously conducted Monte-Carlo simulation results as a training data.

3.1 Preliminaries

In previous chapter, NDI controllers are used to recover F-16 aircraft model from upset conditions. For single loop NDI controller, simulations are carried out for 8 different angle of attack scenarios ranging from 4° to 72° . In all scenarios, body axis angular rates, P, Q, R, are chosen from $[-3.25\text{rad/s}, 3.25\text{ rad/s}]$. As an input to neural network, 6 dimensional vector is used. 3 of these dimensions are the body axis angular rates, 1 of them is the angle of attack and the other two are the quaternion angles which changes with angle of attack. The other 7 states of the aircraft is not used since their initial values are not changed for simulations.

3.2 Neural Network Model

Neural network model is constructed in MATLAB environment using MATLAB's Neural Network toolbox. 2 different model is constructed for 2 different classification scenario. One setting classifies the data into 4 classes whether the regulation is achieved, or velocity limit is violated, or altitude limit is violated, or load factor limit is violated. The other setting is simply splits the data into 2 classes whether the recovery is successful or not. Although the main purpose is to determine the recoverability, 4 class-setting can be used to obtain further information about why the regulation cannot be achieved. For 4 class case, the following neural network, given in Fig. 3.1, is designed with 4 hidden layer consisting 100 neuron each and a 4-neuron output layer.

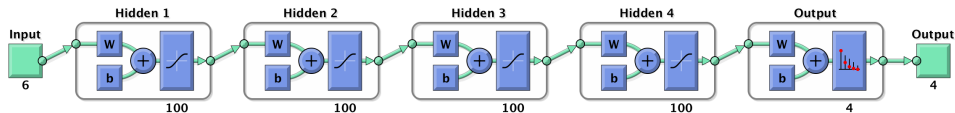


Figure 3.1 : Neural network scheme for 4-class case

Similar network is constructed for 2 class case with 2-neuron output layer which is given in Fig. 3.2.

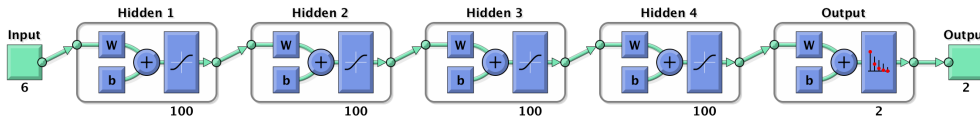


Figure 3.2 : Neural network scheme for 2-class case

Both of the networks are trained using scaled conjugate gradient algorithm and used sigmoid as an activation function. There exists total of 39528 of which the 20% is used for training, 10% is used for validation and remaining 70% is left to test the network. Division of the data performed randomly.

3.3 Results

The motivation of this chapter is to eliminate the computational burden of nonlinear simulations. For that reason, only a small part of the data is used to train the data(20%) with 10% validation. On the other hand, majority of the data is reserved for test(70%). Despite this challenge, networks' success rate reached to satisfactory levels. In Fig. 3.3, neural network achieved to 84.4% success rate on the test data whereas 84.8% success rate on the overall data for 4-class case.

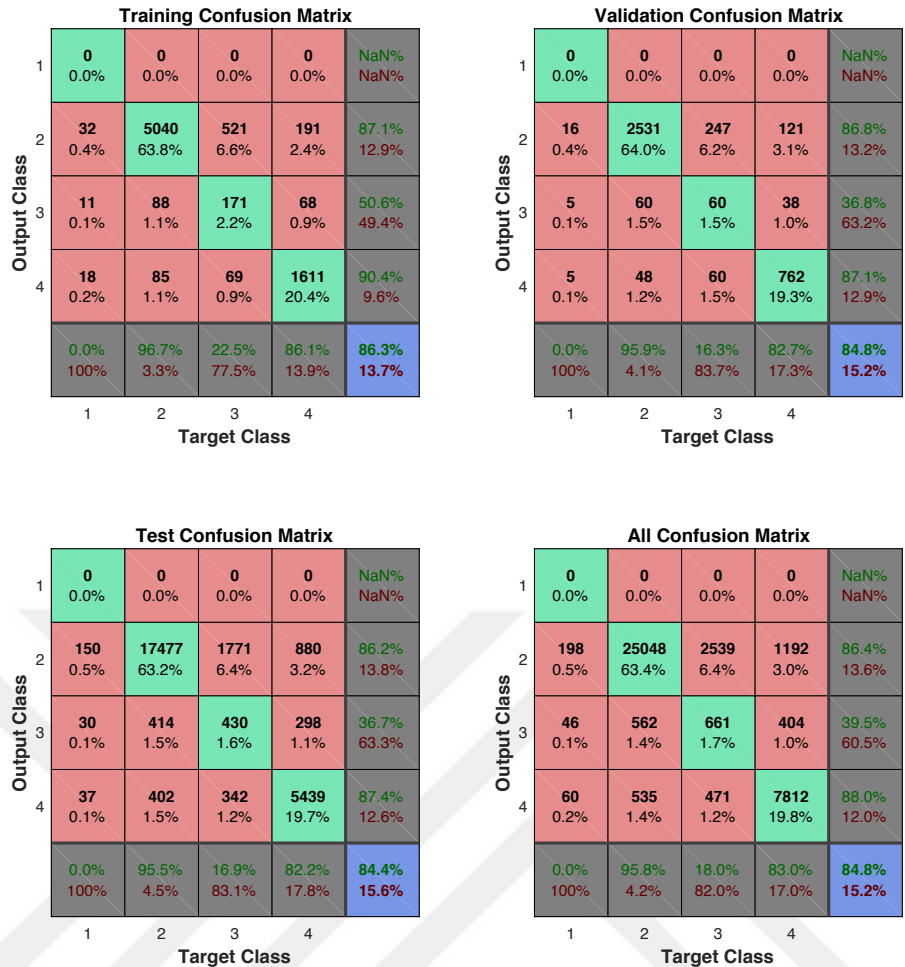


Figure 3.3 : Confusion matrix for 4-class case

In Fig. 3.4, the error distribution is given. As it is seen, most of the data is classified with only 5% error.

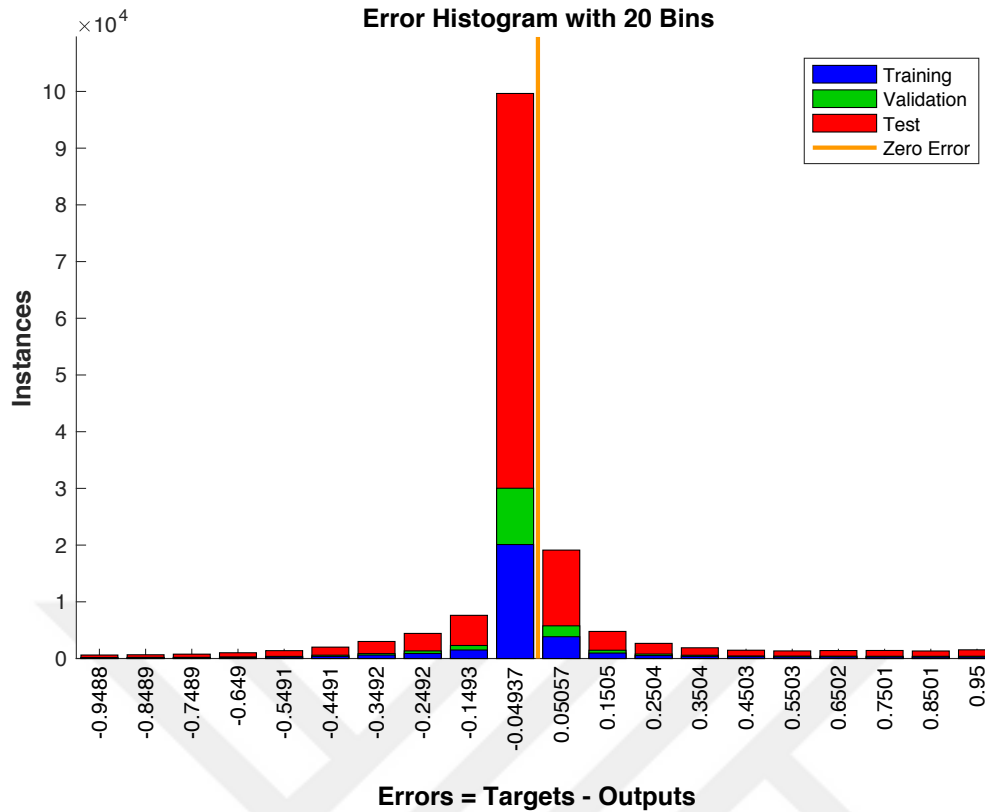


Figure 3.4 : Error distribution for 4-class case

In Fig. 3.5, receiver operating characteristic is given for 4-class case. 4th class which represents the load factor violation has the fastest response since it is highly related to negative pitch rates, which we observe in previous chapter, and therefore the neural network was able to classify it easily. 2nd class which represents the successful regulation has the next fastest response since it is the most frequently observed case.

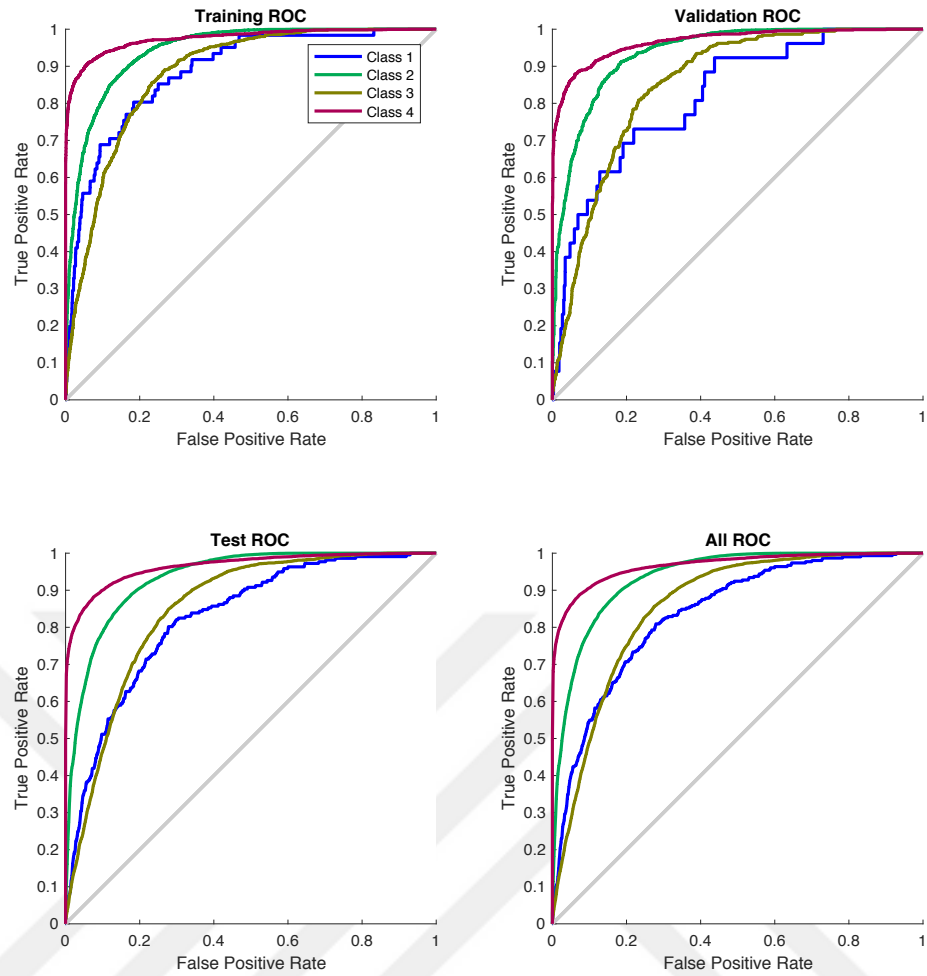


Figure 3.5 : Receiver operating characteristic for 4-class case

Since binary classification is easier, the network for 2-class case achieved better results. As it can be seen in Fig. 3.6, the neural network achieved to 87.1% success rate on the test data whereas 87.6% success rate on the overall data.



Figure 3.6 : Confusion matrix for 2-class case

If we look at the error distribution for 2-class case in Fig. 3.7, we can see that high proportion of the data is classified with under 5% error.

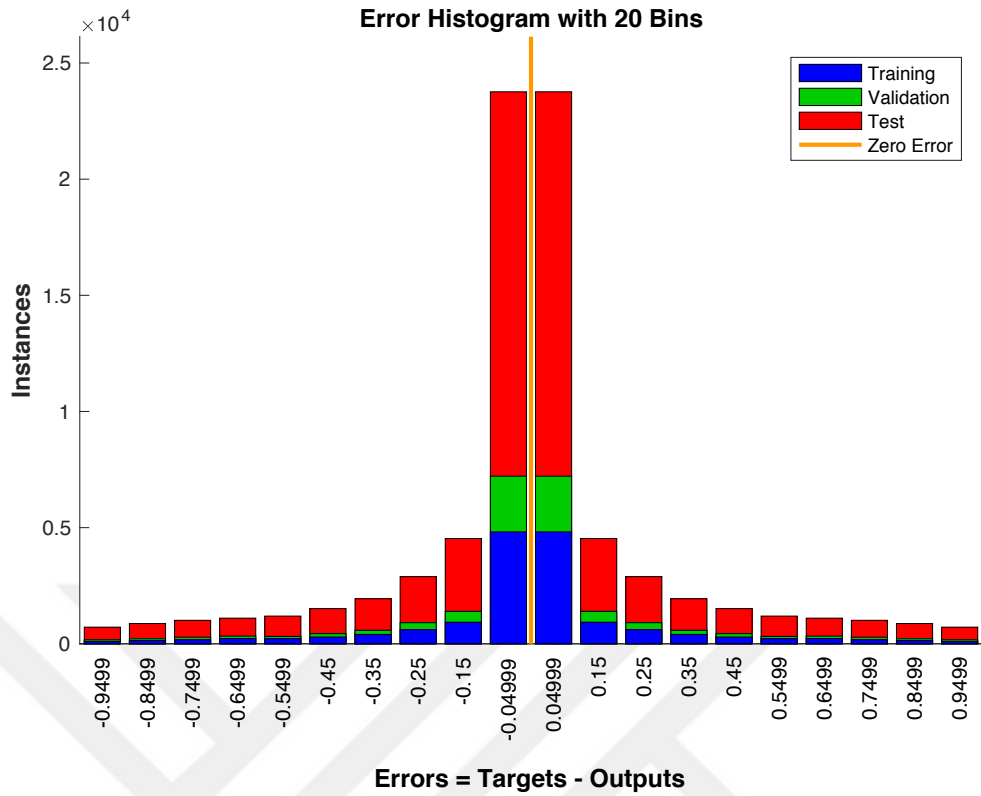


Figure 3.7 : Error distribution for 2-class case

It is due to the reduction of the classes to two by uniting the unrecovered classes in one class. The frequency of the classes became similar. Therefore, the responses seen in receiver operating characteristic in Fig. 3.8 are close to each other.

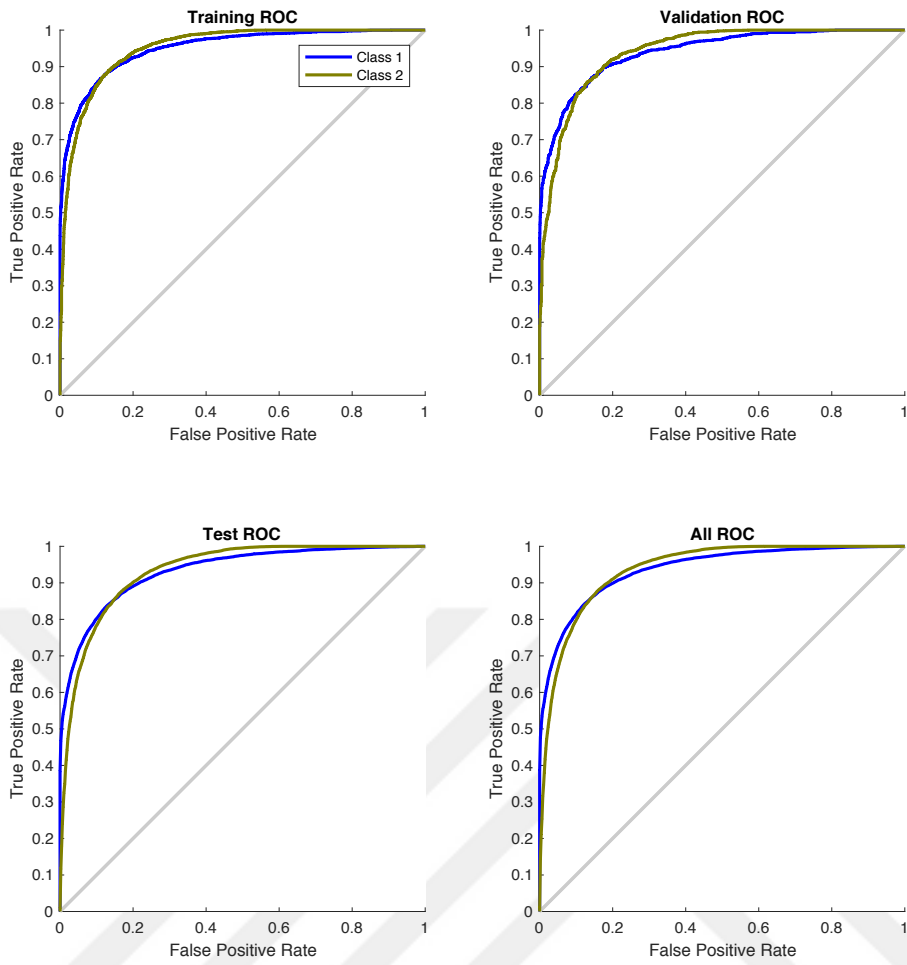


Figure 3.8 : Receiver operating characteristic for 2-class case

4. CONCLUSIONS AND RECOMMENDATIONS

Upset recovery is attempted for the conditions including high angular rates and high angle of attacks by using various controllers which are introduced in content of this work. The control framework is established on a large scale compare to previous works in literature. Based on this framework, comparative study is made for the designed controllers. It is found that nonlinear controllers are superior to linear controllers due to their ability to capture dynamics in harsh conditions. Single loop dynamic inversion controller has been found as the best controller for regulation of high angular rates. In order to have control over aerodynamic angles, double loop dynamic inversion is used. It is shown that this controller is not effective if the high angular rates are present. Therefore, switching NDI controller is proposed to improve the recovery performance. It is found that this controller has superior performance for regulation of angular rates and aerodynamic angles.

In addition, a study made on switching controller to elevate the recovery time performance of the controller. It is observed that selection of switch condition has no linear affect on performance of the controller. Therefore, it brings up an opportunity to derive an optimization problem to consider as a future work.

Moreover, recoverability analysis of an agile maneuvering aircraft is performed using a multi layer neural network. Computational burden of highly nonlinear simulations are eliminated such that the results obtained from nearly forty thousand simulations are reproduced using only 20% of the simulations with around 87% success rate. As a future study, one might study on the optimization of the neural network by tuning the layer and neuron number, improving the training function, finding a better activation function or work on the data to find a smart way to sample it.



REFERENCES

- [1] **Airplanes, B.C.** (2016). Statistical summary of commercial jet airplane accidents: worldwide operations 1959–2015, *Aviation Safety, Boeing Commercial Airplanes, Seattle, WA*. http://www.boeing.com/resources/boeingdotcom/company/about_bca/pdf/statsum.pdf.
- [2] **Abramov, N., Goman, M., Khrabrov, A., Kolesnikov, E., Fucke, L., Soemarwoto, B. and Smaili, H.** (2012). Pushing Ahead-SUPRA Airplane Model for Upset Recovery, *AIAA Modeling and Simulation Technologies Conference*, p.4631.
- [3] **Jacobson, S.** (2010). Aircraft loss of control causal factors and mitigation challenges, *AIAA Guidance, navigation, and control conference*, p.8007.
- [4] **Ranter, H.** (2007). Airliner accident statistics 2006, *Aviation Safety Network*.
- [5] **Fucke, L., Biryukov, V., Grigorev, M., Rogozin, V., Groen, E., Wentink, M., Field, J., Soemarwoto, B., Abramov, N., Goman, M. et al.** (2010). Developing Scenarios for Research into Upset Recovery Simulation, *AIAA Modeling and Simulation Technologies Conference*, p.7794.
- [6] **Team, U.R.I.** (2008). Airplane upset recovery training aid, revision 2, *Federal Aviation Administration & Airline Industry*.
- [7] **Team, A.S.A.J.S.A.** (2014). Final report analysis and results, **Technical Report**.
- [8] **Rao, D.V. and Sinha, N.K.** (2013). A sliding mode controller for aircraft simulated entry into spin, *Aerospace Science and Technology*, 28(1), 154–163.
- [9] **Belcastro, C. and Foster, J.** (2010). Aircraft loss-of-control accident analysis, *AIAA Guidance, Navigation, and Control Conference*, p.8004.
- [10] **Engelbrecht, J.A., Pauck, S.J. and Peddle, I.K.** (2013). A multi-mode upset recovery flight control system for large transport aircraft, *AIAA Guidance, Navigation, and Control (GNC) Conference*, p.5172.
- [11] **Lombaerts, T., Schuet, S., Kaneshige, J., Shish, K.H. and Stepanyan, V.** (2017). Stall Recovery Guidance Using an Energy Based Algorithm, *AIAA Guidance, Navigation, and Control Conference*, p.1021.
- [12] **Sinha, N.K. and KK Venkateswara Rao, D.** (2010). Aircraft spin recovery using a sliding-mode controller, *Journal of guidance, control, and dynamics*, 33(5), 1675–1679.

- [13] **Raghavendra, P., Sahai, T., Kumar, P.A., Chauhan, M. and Ananthkrishnan, N.** (2005). Aircraft spin recovery, with and without thrust vectoring, using nonlinear dynamic inversion, *Journal of Aircraft*, 42(6), 1492–1503.
- [14] **Dongmo, J.E.** (2012). Aircraft Loss-Of-Control Recovery Using Feedback Linearization and High Order Sliding Mode Control, *AIAA Guidance, Navigation, and Control Conference*, p.4548.
- [15] **Crespo, L., Kenny, S., Cox, D. and Murri, D.** (2012). Analysis of control strategies for aircraft flight upset recovery, *AIAA Guidance, Navigation, and Control Conference*, p.5026.
- [16] **Gill, S.J., Lowenberg, M.H., Neild, S.A., Crespo, L.G., Krauskopf, B. and Puyou, G.** (2015). Nonlinear dynamics of aircraft controller characteristics outside the standard flight envelope, *Journal of Guidance, Control, and Dynamics*, 38(12), 2301–2308.
- [17] **Jordan, T., Langford, W., Belcastro, C., Foster, J., Shah, G., Howland, G. and Kidd, R.** (2004). Development of a dynamically scaled generic transport model testbed for flight research experiments.
- [18] **Russell, R.S.** (2003). Non-linear F-16 simulation using Simulink and Matlab, *University of Minnesota, Tech. paper*.
- [19] **Nguyen, L.T.** (1979). *Simulator study of stall/post-stall characteristics of a fighter airplane with relaxed longitudinal static stability*, volume 12854, National Aeronautics and Space Administration.
- [20] **Stevens, B.L., Lewis, F.L. and Johnson, E.N.** (2015). *Aircraft Control and Simulation: Dynamics, Controls Design, and Autonomous Systems*, John Wiley & Sons.
- [21] **Akcal, M.U., Hostas, B., Ure, N.K. and Inalhan, G.** (2018). Recoverability Envelope Analysis of Nonlinear Control Laws for Agile Maneuvering Aircraft, *AIAA Guidance, Navigation, and Control Conference*, p.XXXX.
- [22] **Bryson, A.E.** (1975). *Applied optimal control: optimization, estimation and control*, CRC Press.
- [23] **Slotine, J.J.E., Li, W. et al.** (1991). *Applied nonlinear control*, volume 199, prentice-Hall Englewood Cliffs, NJ.
- [24] **Snell, S.A., Nns, D.F. and Arrard, W.L.** (1992). Nonlinear inversion flight control for a supermaneuverable aircraft, *Journal of guidance, control, and dynamics*, 15(4), 976–984.

CURRICULUM VITAE



Name Surname: Batuhan Hoştaş

Place and Date of Birth: Tekirdağ, 23.09.1991

E-Mail: batuhanhostas@gmail.com

EDUCATION:

- **B.Sc.:** 2016, Istanbul Technical University, Faculty of Aeronautics and Astronautics, Aeronautical Engineering

PUBLICATIONS, PRESENTATIONS AND PATENTS ON THE THESIS:

- Akcal U., Hostas B., Ure N. K., Inalhan G., 2018. Recoverability Envelope Analysis of Nonlinear Control Laws for Agile Maneuvering Aircraft. *AIAA Guidance, Navigation, and Control Conference*, January 8-12, 2018 Kissimmee, Florida
- Yildiz A., Akcal U., Hostas B., Ure N. K., Inalhan G., 2018. Finite State Automata Based Approach to Autonomous Stall and Upset Recovery for Agile Aircraft. *AIAA Guidance, Navigation, and Control Conference*, January 8-12, 2018 Kissimmee, Florida
- Akcal U., Hostas B., Ure N. K., 2018. Rate Envelope Based Time Efficient Strategy for Upset Recovery of a Fighter Aircraft. *IEEE Aerospace Conference*, March 3-10, 2018 Big Sky, Montana